The phosphoinositide signature guides the final step of plant cytokinesis

Alexis Lebecq[1], Camila Goldy[1], Aurélie Fangain[1], Elsa Gascon[1], Katia Belcram[2], Martine Pastuglia[2], David Bouchez[2], Marie-Cécile Caillaud[1*]

[1] Laboratoire Reproduction et Développement des Plantes, Université de Lyon, ENS de Lyon, UCB Lyon 1, CNRS, INRAe, F-69342 Lyon, France.

[2] Université Paris-Saclay, INRAE, AgroParisTech, Institut Jean-Pierre Bourgin (IJPB), 78000, Versailles, France.

*Corresponding author: marie-cecile.caillaud@ens-lyon.fr

One Sentence Summary: The phosphoinositide PI(4,5)P_2 acts as an hallmark to guide the final step of plant cell division.

ABSTRACT

Plant cytokinesis, which fundamentally differs from that in animals, requires the outward expansion of a plasma membrane precursor named the cell plate. How the transition from a cell plate to a plasma membrane occurs remains poorly understood. Here, we report that the acquisition of plasma membrane identity occurs through lateral patterning of the phosphatidylinositol 4,5-bisphosphate PI(4,5)P_2 at the newly formed cell plate membrane. There, the phosphoinositide phosphatase SAC9 emerges as a key regulator, colocalizing with and regulating the function of the microtubule associated protein MAP65-3 at the cell plate leading zone. In *sac9-3* mutant, the polar distribution of PI(4,5)P_2 at the cell plate is altered, leading to ectopic recruitment of the cytokinesis apparatus and formation of an additional cell plate insertion site. We propose that at the cell plate, SAC9 drives the depletion of PI(4,5)P_2 which acts as a polar cue to spatially separate cell plate expansion from the acquisition of plasma membrane identity during final step of cytokinesis.

INTRODUCTION

Cytokinesis is a key cellular process that allows the compartmentalization of living beings into cells, a necessary step for cellular heterogeneity (morphogenesis and differentiation), and in turn for

proprioception (mechanical and biochemical cues channeling organ shape). Plant cytokinesis differs from the unfurrowing cytokinesis observed in animals, and involves the building of a plant-specific cytoskeletal array named the phragmoplast which, by outward growth, drives the separation of the mother cell into daughter cells (*1*). This process requires highly polarized membrane trafficking toward the phragmoplast midzone for the deposition of a transitory membrane structure named the cell plate (*2*). There, overlapping antiparallel microtubules at the outer phragmoplast edge (leading zone, Fig. 1a) drive cell plate expansion toward the cell periphery, while microtubules are disassembled in the inner phragmoplast region (lagging zone). In this process, the most likely microtubule cross-linking factors are proteins in the microtubule-associated protein 65 (MAP65)/Anaphase Spindle Elongation1/Protein Regulator of Cytokinesis1 family and members of the Kinesin-12 subfamily (*3*, *4*). Upon cell plate attachment, a number of changes in cell plate properties and composition occur (*5–7*), suggesting that the leading zone of the phragmoplast might play a role in cytokinesis termination (*8*). The nature of this role remains elusive and the molecular players regulating the transition between cell plate to plasma membrane identity are poorly understood.

Recent evidence points toward a specific anionic lipid signature for the plant plasma membrane (*9*). This landmark is controlled by phosphoinositide metabolism, in particular enzymes such as phosphatases and kinases that locally interconvert the different pools of phosphoinositides (*10*). At the plasma membrane, phosphatidylinositol 4,5-bisphosphate (PI(4,5)P_2) is enriched, whereas PI(4,5)P_2 is excluded from the endocytic pathway (*11*, *12*). This spatial distribution of PI(4,5)P_2 allows polar recruitment of proteins to orchestrate processes such as membrane trafficking (*13–15*) and cytoskeleton remodeling (*16–18*). During cytokinesis, while most anionic lipids accumulate at the cell plate from its inception, PI(4,5)P_2 remains absent (*19*, *20*). Yet, how and when the cell plate acquires a new membrane identity to become a PI(4,5)P_2-enriched plasma membrane remains unknown.

Here we report that PI(4,5)P_2 enrichment at the cell plate occurs upon unilateral attachment to the maternal membrane. At this point, PI(4,5)P_2 remains absent from the leading edge of the phragmoplast at the non-attached side of the phragmoplast, suggesting an active mechanism preventing further passive diffusion. The absence of PI(4,5)P_2 at the leading edge correlates with enrichment of the putative PI(4,5)P_2 phosphatase SAC9. Loss of *sac9* leads to the ectopic accumulation of PI(4,5)P_2 at the phragmoplast leading edge, which correlates with MAP65-3 mis-localization and abnormal cell plate branching starting from the MAP65-3 inner domain at the cell plate. We propose a model in which the absence of PI(4,5)P_2 (or the presence of SAC9) act as a polar cue to guide the leading zone of the phragmoplast during cell plate attachment.

RESULTS

We investigated how PI(4,5)P_2 membrane signature is acquired during cytokinesis, using the Arabidopsis root meristem as a model. Live cell imaging in 3D and time confirmed that during cytokinesis, PI(4,5)P_2 biosensors (mCit-TUBBYc or 2mCH-PH^{PLC})(*11*) are absent from the expanding cell plate until its unilateral attachment to the mother cell (Fig.1A, 1B and Fig. S1, S2). These observations suggest that PI(4,5)P_2-enrichment at the maturing cell plate (Fig.1B, white arrow) probably arises by passive diffusion from the highly fluid lateral plasma membrane of the mother cell.

At this stage, cell plate attachment (blue arrow) is not synchronous along its periphery, allowing to compare attached and non-attached regions of the same cell plate (Fig.1A). At the leading zone of the partially-attached cell plate, where the phragmoplast was still present, a significant decrease of PI(4,5)P_2 biosensor fluorescence (index < 1) was observed (Fig. 1C to 1F and Fig. S1, S3) suggesting an active mechanism preventing PI(4,5)P_2 accumulation to the newly formed membrane domain at the phragmoplast leading zone.

To identify the molecular components driving the exclusion of PI(4,5)P_2 from the leading zone of the expanding cell plate, we analyzed the subcellular localization of the plant-specific enzyme SAC9, which participates in the restriction of PI(4,5)P_2 at the plasma membrane during endocytosis (*21*). We observed that an mCit-SAC9 fusion is enriched at the phragmoplast leading zone (index > 1, Fig. 2A to 2C, yellow arrow, fig. S4, S5), suggesting a role for this enzyme in PI(4,5)P_2 dephosphorylation. To test the direct relationship between the function of SAC9 and the patterning of its substrate PI(4,5)P_2, we mutated the cysteine in the conserved C-x(5)-R-[T/S] catalytic motif found in all SAC domain-containing phosphoinositide phosphatase (SAC9^{C459A}) (*21*). We analyzed the localization of mCit-SAC9^{C459A} likely catalytically inactive and not able to rescue the mutant phenotype (11). We first confirmed that mCit-SAC9 and TdTOM-SAC9^{C459A} colocalized at the leading edge of the cell plate (fig. S6A, B). Like mCit-SAC9, tdTOM-SAC9^{C459A} was enriched at the leading zone while PI(4,5)P_2 was depleted (Fig. 2D to 2F; fig. S6C, D). When SAC9 or the allelic variant SAC9^{C459A} was visualized together with the microtubule associated protein MAP65-3 specifically localizing to the phragmoplast midzone (*22*), a spatial and temporal colocalization at the cell plate leading zone was observed (Fig. 3, fig. S6E to H, movie S1), a feature shared by only a few proteins (*4, 8*).

Our results suggest that active restriction of PI(4,5)P_2 from the leading zone during cell plate attachment is mediated through the enzymatic activity of SAC9. If true, the absence of SAC9 should affect PI(4,5)P_2 distribution at the cell plate. To test this hypothesis, we assessed PI(4,5)P_2 distribution at the cell plate in the *sac9-3* loss of function mutant. In *sac9-3,* PI(4,5)P_2 biosensors are no longer restricted to the plasma membrane, and also ectopically accumulate in endosomes coming from the endocytic pathway (*21*). After unilateral attachment of the cell plate, PI(4,5)P_2 biosensors enrichment at the maturing cell plate was indeed observed both in the WT and in the *sac9-3* mutant. In *sac9-3* we additionally observed an ectopic accumulation of PI(4,5)P_2 biosensors at the leading zone (white

arrowhead), probably being incorporated from cytokinetic vesicles (index >1, Fig. 4A to 3F, fig. S6, S7). Observations in three dimensions revealed that a PI(4,5)P_2 pool was constantly observed on the leading edge of the phragmoplast in *sac9-3* (Fig. 4E). During late cytokinesis in *sac9-3*, the PI(4,5)P_2 pool upfront of the phragmoplast eventually was incorporated to the attached cell plate (Fig. 4E, movie S2). Moreover, the ectopic accumulation of PI(4,5)P_2 biosensor observed in *sac9-3* spatially correlates with the accumulation of the non-functional SAC9^{C459A} at the leading edges of the cell plate, pointing out toward a role of the enzyme in the dephosphorylation of the PI(4,5)P_2 at endosomes(fig. S6, S7). The abnormal PI(4,5)P_2 pattern in the *sac9-3* mutant is consistent with the idea that SAC9 restricts PI(4,5)P_2 and prevents its premature enrichment in the cell plate leading zone (fig. S8). The fact that endosomes rich in PI(4,5)P_2 accumulate at the cell plate leading edge in *sac9-3* cells also suggests that such abnormal PI(4,5)P_2 signature on endosomes originated from endocytosis prevents their fusion with the expanding cell plate (fig. S8). The contribution of the endocytic traffic to plant cytokinesis is still under debate and future research might help us to better characterize this phenomenon. To rule out that the PI4P production through the PI(4,5)P_2 conversion by SAC9 is also involved, we quantified the accumulation of the PI4P biosensor 2xmCH-2xPH^{FAPP1} at the cell plate. No significative difference was observed between the WT and the *sac9-3* mutant, suggesting that only the PI(4,5)P_2 patterning is impaired in absence of SAC9 (fig. S9).

Next, we investigated the functional relevance of the SAC9-dependent PI(4,5)P_2 pattern at the cell plate for cytokinesis. Since phragmoplast organization is regulated by MAP65-3 (*23–26*) that colocalizes with SAC9 (Fig. 3A, 3B; fig. S6E, S6F), we addressed the localization of MAP65-3 in absence of SAC9. During phragmoplast expansion, MAP65-3-GFP dynamics was similar (p.value: 0.00), with a constant MAP65-3 domain of about 2 µm (Fig. 5A, 5B). In WT, MAP65-3 domain gradually decreased in later stages to eventually disappear (Fig. 5A, 5B). In contrast, in *sac9-3* mutant cells, the MAP65-3-GFP domain remained unchanged, at a constant distance of 2.28 µm from the phragmoplast leading edge (Fig. 5A, 5B, movies S3, S4, S5), suggesting a failure to transition to the final stage of cytokinesis in the absence of SAC9.

During defective cytokinesis in *sac9-3*, the persistence of MAP65-3 on the cell plate leading zone always correlated with the emergence of a “branch” from the MAP65-3-GFP inner domain (Fig. 5A, red arrow, fig. S10A). Eventually, the branch labeled by MAP65-3-GFP fused to the maternal membrane at an ectopic site (Fig. 5A, movies S4, S5). On the branch, MAP65-3-GFP behaved as it did in the main phragmoplast, being progressively restricted to the leading zone and ultimately disappearing upon attachment (Fig.5a, movies S4, S5). Quantification of the width/length of the expanding phragmoplast before the first attachment, using RFP-MBD or LifeAct-YFPv as a read out for microtubules and actin respectively, showed no differences between WT and *sac9-3* (fig. S10A to S10G). After cell plate attachment, the microtubule phragmoplast disassembled from the main cell plate

in *sac9-3* as it did in the WT plant (Fig. 5C, fig. S10H to S10J). However, in the branching events observed in *sac9-3*, a pool of microtubules re-engaged as a phragmoplast-like structure on the fully expanded cell plate, at ~2-3µm from the cell plate fusion site, corresponding to the inner face of the MAP65-3-GFP domain (N= 3, red arrow, Fig. 5C, fig. S10J). This finding supports the model in which the phosphoinositide signature coordinates cell plate and microtubule integrity during late cytokinesis.

We tested the genetic interaction between SAC9 and an upstream regulator of MAP65-3, the mitogen-activated protein kinase MPK4 (*27*). MPK4 interacts genetically and physically with the phosphoinositide kinase PI4Kβ1 to control microtubule stability during phragmoplast expansion (*18*). We observed that the *sac9-3,mpk4-2* double mutant is phenotypically indistinguishable from *sac9-3* up to 14 days after germination. Later, *sac9-3,mpk4-2* plants failed to grow and eventually died before giving a progeny (fig. S11). Cell plate branching was not observed in *mpk4*-2 or *map65-3/dyc283*, probably because in these mutants, phragmoplast expansion stops before the complete final attachment, leading to the formation of characteristic cell wall stubs (*22*, *27*, *28*). In the *sac9-3,mpk4* double mutant, the presence of both cell wall stubs characteristics of the *mpk4-2* mutant and of branched cell plates characteristics of the *sac9-3* mutation were detected (fig. S11). Intriguingly, in *mpk4-2* plant complemented with a constitutively active MPK4 kinase ($MPK4^{D198G/E202A}$) (*29*), cell plate branching resembling the one observed in *sac9-3* was observed (around 1.3 defects per root, fig. S11) suggesting that MPK4 activity may be involved in the cell plate branching phenotype observed in absence of SAC9. Whether or not this is directly linked to the function of MAP65-3 still needs to be addressed.

To test our conclusion, we modified the system in a different way. Because the ultimate effector the microtubule cytoskeleton is the main component of the phragmoplast, we reasoned that microtubule disruption could lead to a similar phenotype. We then tested the sensitivity of *sac9-3* to mild perturbations of the cytoskeleton using pharmacological treatments (fig. S12). In plants treated with 1 µM Taxol (fig. S12 A, B) or 1.5 µM propyzamide (fig. S12 C, D) root growth reduction was similar in *sac9-3* and in the WT. At the subcellular level, WT plants grown on 1 µM Taxol or 1.5 µM propyzamide did not display detectable cytokinesis defects (fig. S12 B, D). At higher concentrations (25 µM and 50 µM respectively for 24 h) cell plate branching was detected in WT, as well as after treatment with 20 µM Chlorpropham (fig. S13A, B). Perturbation of the actin cytoskeleton using 0.1 µM Latrunculin B for 24 h did not induce the formation of branched cell plate, which might suggest that this phenomenon does not require directly actin cytoskeleton integrity (fig. S12E, F; fig. S13 B). In contrast to *sac9-3*, cell plate branching induced by microtubule drugs often emerged before first attachment (fig. S13A), highlighting a broader effect of the drugs on phragmoplast expansion. In WT plants treated with 25 µM Taxol, MAP65-3-GFP decorated microtubules of the branched phragmoplast, whereas in *sac9-3*, localization of MAP65-3-GFP was restricted to the phragmoplast midzone (Fig. 5A, fig. S13C). However, in all cases, enrichment in MAP65-3-GFP was observed at the initiation site of the branch

(Fig. 5A, fig. S13B, C). Based on our findings, we conclude that the phenotype observed in *sac9-3* might not result from defects in microtubule dynamics and phragmoplast expansion *per se*, but rather from defective perception of cell plate attachment, resulting in ectopic reactivation of the phragmoplast.

Using KNOLLE localization as a readout for cell plate fusion defects (*8*, *30*, *31*), we showed that in contrast to what was previously reported for mutations impairing membrane fusion, no dispersed vesicular localization was observed for YFP-KNOLLE in *sac9-3* (Fig. S14). Moreover, YFP-KNOLLE decorated the branching cell plate indicating that this ectopic membrane domain has a cell plate identity (Fig. 5D, 6A). Abnormal branching represented 4% of the total apicobasal cells walls (~11 cells/root n = 30 roots, N = 3 replicates), which is comparable to what is often observed for mutant impaired in cytokinesis (*18*, *32*). Cell wall defects observed in *sac9-3* were exclusively positioned at the crosswall in proximity to the mother cell lateral wall, with an intersection relatively constant at 2.93 µm ± 0.91 SD (Fig. 6B to 6D, movies S8, S9), reminiscent of the distance labeled by MAP65-3-GFP and mCit-SAC9 at the phragmoplast leading zone in WT (Fig. 3, Fig. 6B white asterisk, fig. S5).

To determine if the phenotype observed was due to mis- positioning of the cell division site, we analyzed the position of the preprophase band using our MAP65-3 marker as a readout (*28*, *33*). We imaged MAP65-3-GFP in *sac9-3* dividing cells, from early mitosis to late cytokinesis, using our root tracking system (*34*). While the first attachment of the cell plate indeed corresponds to the position previously occupied by the PPB, no MAP65-3-GFP signal was observed at ectopic attachment sites in *sac9-3* (fig. S15A). According to the existing model, the cell plate attachment site within the cortical division zone is facilitated by a set of specialized proteins (2). We assessed localization of the cortical division zone marker PHRAGMOPLAST ORIENTING KINESIN 1 (POK1) (*35*). In absence of SAC9, YFP-POK1 was observed at the cortical division zone in two distinct spots (blue arrows) corresponding to the first attachment site, but also at the abnormal second cell plate attachment site observed in *sac9-3* defective cytokinesis (fig. S15B). This finding suggests that in absence of SAC9, the cell plate extension, and its guidance is reactivated leading to the formation of an abnormal branched cell plate.

To test the temporal specificity of this phenotype, we reasoned that a transient rescue may be sufficient. By engineering a construct fusing SAC9 to the expression, localization and degradation signals of MAP65-3 (*25*) we were able to mitotically express SAC9, target it to the cell plate and degrade it after mitosis (fig. S16). Using this construct, we showed that expressing *SAC9* during mitosis was sufficient to rescue the *sac9-3* cytokinesis defect as well as part of its dwarf phenotype, highlighting the importance of SAC9 function during cell division. However, we cannot exclude the possibility that the mitotic expression of SAC9 may be sufficient to restore $PI(4,5)P_2$ distribution at the plasma membrane in later stages, thereby complementing aspects unrelated to cell division as well.

Concomitantly to the cell plate-branching in *sac9-3*, a specific distribution of PI(4,5)P_2 biosensor was observed, with a burst i) at the cell division site where the cell plate attached, ii) on the cell plate, at ~ 3 µm where the branching was initiated, iii) and at the ectopic cell division site where the cell plate-branched was inserted (N = 5, white arrowhead, Fig. 6E, fig. S17, movie S10). Moreover, mCit-*SAC9*^{C459A} was not able to rescue the phenotype observed (fig. S18). Altogether, our findings suggest that the phosphatase activity of SAC9 (and thereby its role the PI(4,5)P_2 repartition) is critical to coordinate cell plate attachment through MAP65-3 behavior.

DISCUSSION

Cytokinesis in multicellular organisms dictates how cells are organized in a tissue, their identities, and their functions. At the heart of cytokinesis, the coordination between the cytoskeleton and the vesicle trafficking is of paramount importance as it drives the separation of the mother cell into daughter cells. In this context, an extensive number of studies on the role of proteins implicated in the cytoskeleton's remodeling and trafficking have been reported (*36*). Yet, the mechanism by which the final step of cell division occurs remains unclear.

Here, we took an unexplored angle, looking at the role of membrane lipids during the final steps of cytokinesis. Using Arabidopsis as model, we showed that the anionic lipid signature controls cytokinesis in plants. This analysis was possible thanks to the identification and characterization of a class of mutants in which the last step of cytokinesis is not perceived. In this mutant, which is impaired in phosphoinositide metabolism (*21*), defects during the final step of cytokinesis provoke abnormal multiple-cell division sites in a given cell. The branching of the cell plate is to our knowledge a rare phenomenon that has been only observed after mild perturbation of the microtubule cytoskeleton (this study) or in the conditional mutant *mor1-1* (*37*). This mutant, impaired in a member of the XMAP215 family of microtubule-associated proteins displays at restrictive temperature branched cell plates but also incomplete, asymmetric, wandering cell plates (*37*). The stereotyped branched cell plates observed in absence of SAC9 appears therefore more specific than a general disruption of the microtubule cytoskeleton. We wondered whether the aberrant branching observed in *sac9* preferentially occurs at the unattached phragmoplast side after unilateral attachment. However, due to the technical limitations of live cell imaging in four dimensions in the native tissue, we cannot answer this point in a quantitative manner.

We showed that the cell plate branching observed in absence of SAC9 does not result from a PPB positioning defect but is rather linked to the formation of a secondary cortical division zone where YFP-POK1 is enriched. We showed that after pharmacological perturbation of microtubules arrays in the

sac*9-3* mutant, the branching of the cell plate always coincided with the enrichment in MAP65-3-GFP at the site of initiation. Because of technical limitations, we are not able to know if the signal observed for POK1 at the abnormal second cell plate attachment site appears early during mitosis or later during the cell plate branching. If POK1 was present in early division at two sites, the first attachment is *sac9-3* should occur at 50 % in on site and 50 % at the other site where POK1 is accumulating. This would lead to a phenotype characterized by tilted cell plates (*38*, *39*). Since the quantification of the arrangement of cell walls perpendicular to the growth axis show no difference between *sac9-3* and WT (fig. S19), we hypothesize that POK1 accumulation at the ectopic cortical division zone is more likely appearing in late cytokinesis.

We found that SAC9 progressively disappears from the fully attached cell plate upon its unilateral attachment to the mother cell. Consequently, SAC9 does not localize to the plasma membrane in the resulting interphasic cells (*21*). Hence, SAC9 and its substrate are mutually co-excluded spatially. Our previous work suggests that SAC9 function is more likely restricted to endosomes emerging from the plasma membrane during endocytosis than directly at the plasma membrane (*21*). We therefore do not expect the PI(4,5)P_2 level to increase at the plasma membrane or at the maturing zone of the cell plate. We rather think that SAC9 mutation most likely affects the ratio between the PI(4,5)P_2 at the plasma membrane and the internalized PI(4,5)P_2. This is why the PI(4,5)P_2 biosensors which are expressed at a similar level in WT and *sac9-3*, are mainly labeling the pool of PI(4,5)P_2 in endosomes rather than the PI(4,5)P_2 pool present at the plasma membrane (*21*). This phenomenon is extreme for the TUBBYc biosensor, but the use of two independent biosensors to detect the PI(4,5)P_2 used in this study allows us to observe a consensus localization at the leading edge of the cell plate for the PI(4,5)P_2 biosensors in absence of SAC9.

To test the direct relationship between the function of SAC9 and the patterning of its substrate the PI(4,5)P_2, we generated a catalytic dead version of SAC9 (*21*). Here, we showed that while *sac9-3* is complemented with *SAC9pro:mCit-SAC9*, the expression of *SAC9pro:mCit-SAC9*^{C459A} was not sufficient to rescue the cytokinesis defects observed in *sac9-3*. We previously confirmed that mCit-SAC9^{C459A} fusion was stable and accumulated to a similar extent as mCit-SAC9 (*21*). Since the putative catalytic cysteine, C459, is required for SAC9 function during cytokinesis, we can conclude that the phosphatase activity of SAC9 is participating in the observed phenotype. Given that phosphoinositide's metabolism is highly intricate, we recognize that it is difficult to fully untangle the specific involvement of each lipid in the observed phenotypes. Moreover, SAC9 may carry specific functions outside of its catalytic activity, and therefore the phenotype observed could be due to other factors, such as the recruitment of protein partners.

Since both SAC9 and the allelic variant mutated in the catalytic site are both recruited to the leading edge of the cell plate and to membrane in interphasic cells, we speculate that SAC9 targeting to

membrane is regulated by interaction with a protein partner rather than by its substrate. Because of the co-localization between SAC9 and MAP65-3 and the phenotype observed in constitutively active MPK4, it is tempting to speculate that these proteins might be interacting. However, since SAC9 is recruited to membranes in both interphasic and dividing cells, we rather suspect protein partners not specifically expressed during mitosis. Hence, Ras-associated binding (RABs), small guanosine triphosphatases regulating protein transport along the endocytic and exocytic pathways are good candidate to regulate SAC9 localization. This phenomenon is well known in animal cells, where the functional homologs of SAC9, the PI(4,5)P_2 5-phosphatase OCRL is recruited to membranes during cytokinesis via its interaction with RAB35 (*40*).

Numerous evidence coming from the animal literature highlights the connection between the PI(4,5)P_2/PI4P balance, to the function and the recruitment of actin-binding proteins and actin nucleators (*41*). In plants, little is known about the role of the actin cytoskeleton during cytokinesis and the link with the phosphoinositide metabolism in the context of mitosis is also hypothetical. The increased number of defects observed in the *sac9-3* mutant after disruption of the actin cytoskeleton (fig. S12F) suggests a crosstalk between the phosphoinositide metabolism and the actin cytoskeleton during cell plate attachment. Whether or not the accumulation of PI(4,5)P_2 endosomes promote F-actin polymerization and perturb polarity/cell plate behavior in the sac9-3 remains to be addressed in further detail in the future.

Using PI(4,5)P_2 biosensors, we observed that PI(4,5)P_2 is depleted from the leading edge of the cell plate, where SAC9 restricts its patterning. Passive diffusion of PI(4,5)P_2 or more generally high PI(4,5)P_2 may induce a switch in microtubule dynamics to stop phragmoplast expansion. It was recently shown that upon PI(4,5)P_2 inactivation using an inducible PI(4,5)P_2 depletion system, highly anisotropic transverse cortical microtubules were replaced by randomly arranged arrays, suggesting a function of PI(4,5)P_2 in the organization of microtubules in plant cells. Active exclusion of PI(4,5)P_2 at the unattached leading end of the phragmoplast may thus be required to maintain microtubule dynamics until the successful completion of cytokinesis.

We observed that SAC9 undergoes the exact same changes in localization as MAP65-3, first enriched on the entire cell plate (disk phragmoplast stage), then accumulated at the leading edges and absent at the center of the maturing cell plate. The fact that SAC9 accumulates at the cell plate at an early stage might suggest that PI(4,5)P_2 accumulation is actively restricted at the expanding edge. Even though we cannot rule out that SAC9 has another function during the early phases of phragmoplast formation, the phenotype observed in *sac9* suggests that SAC9 function is required during the cell plate attachment, preventing the premature accumulation of the PI(4,5)P_2 at the growing leading edges.

It is plausible that during cell plate attachment, SAC9 is important for vesicle fusion. In this case, the additional cell plate attachment sites could be caused by abnormal fusion of vesicles or membrane remodeling in addition to changes in the phosphoinositide signature. Yet, no dispersed vesicular localization was visible in the *sac9-3* mutant using confocal microscopy (this study) and electron microscopy (*42*), suggesting that the additional cell plate attachment sites is probably not caused by abnormal fusion of vesicles. Fusion defects during cytokinesis often result in multinucleated cell formation (*43*, *44*) which was also not observed in *sac9-3* (*42*). When we compared the already published electron micrograph of *sac9-3* (*42*) with the micrograph of mutants impaired in membrane fusion (*30*, *45*, *46*), the characteristic fusion defect phenotype is not visible in *sac9-3* while cell wall protuberances emerging from the cell plate are clearly visible (*42*). Altogether, our confocal imaging and already available *sac9-3* electron micrograph do not support classical defects in the vesicular fusion at the cell plate. The phenotype observed in *sac9-3* electron micrographs resembles what was reported for the microtubule-associated protein mutant *mor1-1* in which bifurcated cell plates and abnormal cell wall structures were observed (*37*), suggesting that SAC9 might function in a pathway together with component of the microtubule cytoskeleton. It might be the case that the abnormal PI(4,5)P_2 containing endosome observed around the leading edge in *sac9-3* failed to be incorporated to the cell plate because of their abnormal membrane identity. Future direction should better address the fusion of the cell plate with the plasma membrane. So far, while the homotypic fusion of vesicles during cell plate expansion is well described (*47*), the mechanism allowing the fusion of the cell plate to the plasma membrane is poorly documented. To our knowledge, only one study refers to this phenomenon (*48*). In this paper, the loss of the clathrin-mediated endocytosis adaptor *TPLATE* by RNAi in BY-2 cell lines leads to "anchoring" defects of the cell plate. In this case, fusion defects are associated with the massive recruitment of material/vesicles, close to the cell plate insertion site (*48*). Based on the current knowledge, we cannot exclude that *SAC9* plays a role during the fusion of the cell plate with the plasma membrane. Nonetheless, the phenotype observed in TPLATE RNAi cells (*48*) differs from what we observed in absence of SAC9, which might indicate that SAC9 is important for dephosphorylating PI(4,5)P_2 at/close to the cell plate edges rather than vesicle fusion. It is tempting to suggest that the cell plate fusion to the plasma membrane allows for fusion of heterogeneous material as PI(4,5)P_2 containing endosomes. If true this may explain why cytokinesis defects appears only at this stage in *sac9-3* and also differences observed with microtubules destabilizing drugs. Future directions should include the identification of the molecular machinery controlling the cell plate fusion with the plasma membrane.

We propose that upon unilateral cell plate attachment to the plasma membrane, polarity domains (ie. cell plate maturing domain versus cell plate leading edges) are formed and the phragmoplast lagging zone acts as a buffer between the PI(4,5)P_2 enriched maturing zone and the still expanding cell plate leading edge. In absence of SAC9, the presence of PI(4,5)P_2 upfront of the phragmoplast might perturb the function of cytoskeleton components such as MAP65-3, provoking the reassembly of the

phragmoplast apparatus on the inner side of the leading zone. An alternative model could be that the accumulation of PI(4,5)P_2-rich endosomes close to the leading edge but disconnected from the cell plate, influences cell plate growth and branching in the *sac9-3* mutant. In any case, our findings support the model by which the absence of PI(4,5)P_2 (or the presence of SAC9) might act as a polar cue to guide the leading zone of the phragmoplast at the final step of the plant cytokinesis (fig. S20).

MATERIALS AND METHODS

Growth condition and plant materials

Arabidopsis thaliana Columbia-0 (Col-0) accession was used as a wild-type (WT) reference genomic background throughout this study. All transgenic lines used in this study are listed in supplementary table A. Arabidopsis seedlings were grown in vitro on half Murashige and Skoog (½ MS) basal medium supplemented with 0.7% plant agar (pH 5.7) in continuous light conditions at 21 °C. Seedlings were imaged between 5 and 7 day after germination (dag) and finally grown in soil under long-day conditions at 21 °C and 70% humidity 16 h daylight. For drugs treatments, wild type and *sac9-3* seedlings were grown in vitro for 6 days and then transferred on ½ MS basal medium supplemented with 0.7% plant agar and either 20 µM of Chlorpropham or 25µM Taxol, 50µM Oryzalin, 10µM Propyzamide, 5µM Latrunculin B. Images were taken after 24h of incubation. For root growth experiments, *sac9-3* and wild type seedling were grown, after 3 days at 4°C in the dark, on ½ MS plates supplemented with various concentrations of drugs: 1 µM Taxol, 1.5 µM Propyzamide or 0.1µM Latrunculin B for 7 days.

Cloning and plant transformation

Cloning of MAP65-3pro::2xmTU2-MAP65-3: The MAP65-3pro (1,2 kb) was flanked with attB2R and attB3 sequences and recombined by BP gateway reaction into pDONR221 (Fw: GGGGACAACTTTGTATAGAAAAGTTGCTTACACTCTTCCCTACACAAAACCGCG ; Rv: GGGGACTGCTTTTTTGTACAAACTTGCTTCGAAATGCTTAAGCCTGTAACAGG). Final destination vectors (MAP65-3pro/P5', MAP65-3/pDON207 (*28*), 2xmTU2/pDONR-P3') were obtained using three fragments LR recombination system (ThermoFisher scientist, www.thermofisher.com) using pK7m34GW destination vector (*49*).

The collection of phosphoinositide biosensors used in this study was described previously (*11*). A tandem dimer of the monomeric red fluorescent protein CHERRY (2xmCH) (*50*) was used to generate

a stable transgenic Arabidopsis line to increase the poor signal obtain in red, in particular, because of the autofluorescence of the plant tissue.

The swapping domain was engineered using a vector containing mCitrine (mCit), cYFPnoSTOP/pDONR221 (previously described by (*11*)), and a vector containing MAP65-3 (*28*) . The C-terminal domain 2 of MAP65-3 (MAP65-3^{Cter}; EALYGSKPSPSKPLGGKKAPRMSTGGASNRRLSLGAAMHQTPKPNKKADHRHNDGALSNG RRGLDIAGLPSRKQSMNPSEMLQSPLVRKPFSPISTTVVASKANIATTTTQQLPKNNAVNEISS FATPIKNNNILRNLEEEKMMTMMMQTPKNVAAMIPIPSTPATVSVPMHTAPTPFTNNARLMS EKPEVVEYSFEERRLAFMLQSECRLV) was amplified by PCR (*25*): FW: ccaactttgtacaaaaaagcaggctttaaccatggaggcactttacgggtccaaaccc; Rv: gaacagctcctcgcccttgctcaccataaccaaacgacattcagactgtagcatgaa) and introgressed into cYFPnoSTOP/pDONR221 by Gibson cloning (primer FW: ccttcatgctacagtctgaatgtcgtttggtaatggtgagcaagggcgaggagctgt Rv: gctgggtttggacccgtaaagtgcctccatggttaagcctgctttttgtacaaagtt). Then by directed mutagenesis we add an ATG before MAP65-3^{Cter} sequence (primer FW:gcaggcttaaccATGgaggcactttacggg Rv:cccgtaaagtgcctcCATggttaagcctgc). MAP65-3^{Cter} -cYFPnoSTOP/pDONR221vector was used to obtain final destination vectors using three fragments LR recombination system (ThermoFisher scientist, www.thermofisher.com) using pB7m34GW destination vector (*49*), pDONR-P4-P1R containing MAP65-3 promotor and pDONOR-P2R-P3 containing SAC9.

Wild-type Col-0 and heterozygous (or homozygous) *sac9-3* were transformed using the dipping method (*51*). For each construct generated in this paper, between 20 and 24 independent T1 were selected on antibiotics and propagated. In T2, all lines were screened using confocal microscopy for fluorescence signal and localization. Between 3 to 5 independent lines with a mono-insertion and showing a consistent, representative expression level and localization were selected and grown to the next generation. Each selected line was reanalyzed in T3 by confocal microscopy to confirm the results obtained in T2 and to select homozygous plants. At this stage, we selected one representative line for in depth analysis of the localization and crosses and two representative lines for in depth analysis of mutant complementation.

Live cell imaging

Time-lapse imaging on living root tissues were acquired either manually, or using an automated root tracking system set-up previously (*34*). Briefly, plants roots expressing fluorescent proteins were imaged with a spinning disk confocal microscope while they grow using automatic movement of the

microscope stage that compensates for root growth, allowing the imaging of the dividing cells in the root meristem over time (*34*). For both type of experiment, Z-stacks were acquired every 1 min to 3 min with the following spinning disk confocal microscope set up: inverted Zeiss microscope (AxioObserver Z1, Carl Zeiss Group, http://www.zeiss.com/) equipped with a spinning disk module (CSU-W1-T3, Yokogawa, www.yokogawa.com) and a ProEM+ 1024B camera (Princeton Instrument, www.princetoninstruments.com/) or Camera Prime 95B (www.photometrics.com) using a 63x Plan-Apochromat objective (numerical aperture 1.4, oil immersion). GFP and mCit were excited with a 488 nm laser (150 mW) and fluorescence emission was filtered by a 525/50 nm BrightLine! a single-band bandpass filter (Semrock, http://www.semrock.com/), mCHERRY and TdTOM were excited with a 561 nm laser (80 mW) and fluorescence emission was filtered by a 609/54 nm BrightLine! a single-band bandpass filter (Semrock). For quantitative imaging, pictures of epidermal root meristem cells were taken with detector settings optimized for low background and no pixel saturation. Care was taken to use similar confocal settings when comparing fluorescence intensity or for quantification. In this study, we used PI4P biosensors as a general marker for endomembrane as it localizes both to plasma membrane and Trans-Golgi Network (*19*). This allows the visualization of both the plasma membrane and the cell plate (*19*), in *sac9-3* and WT plants. We are not expecting a change in behavior for this biosensor in *sac9-3* as we observed the same localization in the WT (*21*). For the double localization of the membranes and the microtubules in sac9-3 using time-lapse imaging, the fact that both markers are tagged with similar fluorophores is not optimal. In fact, we were only able to rescue plants for the cross *sac9-3*$^{-/-}$ x RFP-MBD. Then we tried to introduce a third construct in *sac9-3*$^{-/-}$ x RFP-MBD with a mCit tagged membrane marker, but we did not succeed. Therefore, because of technical limitations, we analyzed the line expressing sac9-3$^{-/-}$ x RFP-MBD x 2xmCh-2xPH^{FAPP1} and the corresponding RFP-MBD x 2xmCherry-2xPH^{FAPP1} in WT.

Calcofluor staining and immunolocalization imaging

For calcofluor staining, root meristem cell walls were stained using the calcofluor dye, following the protocol described in (*52*). Seedlings were incubated overnight in a fixation buffer (50% of methanol, 10% of acetic acid, and 40% of distilled water). The seedlings were then rehydrated in ethanol baths for 10 min each: 50% ethanol, 30% ethanol, and distilled water twice. Afterward, the seedlings were transferred in the staining solution for overnight incubation (90% of clearsee solution (5% of urea, 15% of deoxycholic acid, and 10% of xylitol in distilled water) and 10% of calcofluor white solution (500 mg Fluorescent Brightener 28 in distilled water (qsp 50mL) and 1 drop of NaOH 10N). Before imaging, the seedlings were rinsed for 15 min in clearsee solution. For segmentation and tissue localization of the defects, z-stacks were performed with 0.39 µm space between acquisitions. For *sac9-3* defects

comparison with MAP65-3^{Cter} complementation experiments, z-stacks were performed with 0.8 to 1µm space between acquisitions.

Whole-mount immunolocalization was performed as described (*53*). For immunolocalization, seedlings were fixed in 4% paraformaldehyde and 0.1% Triton X-100 in ½ MTSB buffer (25 mM PIPES, 2.5 mM MgSO4, 2.5 mM EGTA, pH 6.9) for 1 h under vacuum, then rinsed in PBS 1X for 10 min. Samples were then permeabilized in ethanol for 10 min and rehydrated in PBS for 10 min. Cell walls were digested using the following buffer for 1 h: 2 mM MES pH 5, 0.20% driselase and 0.15% macerozyme. Tissues were incubated overnight at room temperature with the B-5-1-2 monoclonal anti-α-tubulin (Sigma) and the anti-KNOLLE antibody (kind gift of G. Jürgens, University of Tübingen, Germany (*45*)). The next day, tissues were washed for 15 min in PBS, 50 mM glycine, incubated with secondary antibodies (Alexa Fluor 555 goat anti-rabbit for KNOLLE antibody and Alexa Fluor 488 goat anti-mouse for the tubulin antibody) overnight and washed again in PBS, 50 mM glycine. Samples were incubated in 10% calcofluor white solution for 2 h and then mounted in VECTASHIELD.

Imaging was performed on an inverted Zeiss CLSM800 confocal microscope using a 40x Plan-apochromatic objective. Dual-color images were acquired by sequential line switching, allowing the separation of channels by both excitation and emission. GFP was excited with a 488 nm laser, mCIT was excited with a 515nm laser, mCH/tdTOM were excited with a 561 nm laser and finally Fluorescent Brightener 28 (Calcofluor) was recorded using a 405 nm excitation.

Super resolution microscopy

For imaging mCit-SAC9 in fixed tissue, seedlings expressing mCit-SAC9 were fixed in 4% paraformaldehyde and 0.1% Triton X-100 in ½ MTSB buffer (25 mM PIPES, 2.5 mM MgSO4, 2.5 mM EGTA, pH 6.9) for 1 h under vacuum, then rinsed in PBS 1X for 10 min. Samples were then permeabilized in Methanol for 10 min and rehydrated in PBS for 10 min. Cell walls were digested using the following buffer for 1 h: 2 mM MES pH 5, 0.20% driselase and 0.15% macerozyme. Tissues were incubated overnight at room temperature with the B-5-1-2 monoclonal anti-α-tubulin (Sigma). The next day, tissues were washed for 15 min in PBS, 50 mM glycine, incubated with secondary antibodies (Alexa Fluor 555 against the B-5-1-2 monoclonal anti-α-tubulin and with the GFP-Booster Atto647 antibody) overnight and washed again in PBS, 50 mM glycine. Samples were incubated in 10% calcofluor white solution for 50 min and then mounted in 80% Citifluor AF1.

High resolution imaging was performed using a LSM980 Airyscan2 (ZEISS) using a 40x objective (numerical aperture 1.3, oil immersion). Dual-color images were acquired by sequential line switching, allowing the separation of channels by both excitation and emission. GFP-Booster, mCitrine, mTU2

and Fluorescent Brightener 28 (Calcofluor) were excited using 639 nm, 514nm, 445 nm and 405nm lasers respectively. All the signals were recorded with an airyscan 2 detector except Fluorescent Brightener 28 for which a PMT was used. Airyscan processing was performed with ZEN imaging software (ZEN blue).

Root growth quantification

Plants growth was manually measured using ImageJ at 7-day post germination. For each drug 3 independent biological replicates were analyzed (2 for Latrunculin B) with each time three technical replicates.

Segmentation and tissue localization of *sac9-3* defects

Quantification of cell division defects was based on manual counting of full Z-stacks with a z-spacing equal to the lateral resolution in order to get cubic voxels allowing to quantify the defects, number, and position in the tissue, with the ImageJ orthogonal view plugin (or z-spacing of 0.5 and 1µm in cases that only defects count was needed). Segmentation was performed using ImageJ, (morphological segmentation) plugin as described and angle extraction using ImageJ plugin developed (*54*).

The *sac9-3* defects architecture was manually measured using ImageJ, “straight line” and “angle tool” tools, and data were analyzed with excel.

Fluorescence intensity extraction and localization indexes (fig. S21)

<u>Normalized fluorescence intensity</u>: was obtained using Fiji tool, extracted from 10 dividing cells (cells of an approximatively equivalent length, normalized to the exact same size by suppressing a part of the space between the cell plate and plasma membrane (Disk phragmoplast) or just the exact same length on only one expanding edge (discontinuous phragmoplast), normalized by the intensity at the cell plate center (except for fig. S4 and S5 where the normalization was by the cytosolic intensity), and plotted to obtain an average intensity profile.

<u>For PI(4,5)P_2 localization index on the discontinuous phragmoplast:</u> phragmoplast length was measured and divided into two equal parts, the leading zone (domain close to the plasma membrane) and the lagging zone (domain close to the cell center). Fluorescence intensity was measured on each zone of

the phragmoplast and, in addition, on the entire cell plate and cytosol. Next, the cytosol intensity background was subtracted and, finally, the leading and lagging zones were divided by the global cell plate intensity. The final ratio superior to 1 underlined an enrichment at a specific zone of the phragmoplast. The final ratio inferior to 1 underlines the depletion.

SAC9-PI(4,5)P_2 localization index on the discontinuous phragmoplast: To address mCit-SAC9 and tdTOM-SAC9^{C459A} co-exclusion with PI(4,5)P_2 biosensor we used the same index as the PI(4,5)P_2 localization index. Because we showed that the PI(4,5)P_2 biosensor was excluded from the leading zone, when a microtubule marker was not present in the imaged transgenic line, we decided to use the PI(4,5)P_2 biosensor as a separation between the leading and lagging zone. Using PI(4,5)P_2 biosensor fluorescence decrease as a marker of this separation, we measured the intensity on 1.5 µm (the approximative half-length of the phragmoplast) on each side of PI(4,5)P_2 biosensor limit. Finally, the leading and lagging zones were divided by the intensity of the cell plate and nearby cytoplasm (1µm around the cell plate).

MAP65-3 labeling distance: Measurement was performed using ImageJ, a “straight line” tool every two minutes on one side of the cell plate (the one with the persistent pool in *sac9-3*). Lines were created between the outer and inner MAP65-3 on the entire length labeled. The lengths were plotted relative to the "disk"-"ring" phragmoplast transition (0 min) and cell plate attachment (14 min).

PI(4,5)P_2 phragmoplast accumulation index: One dividing cell and one of its surrounding non-dividing cells were taken for each root. For every two cells, the signal intensity was measured in one elliptical region of interest (ROIs) at the phragmoplast (around the cell plate across all cell lengths or at the equator of interphasic cells), with an equal area between the two cells. In addition, we measured signal intensity at the plasma membrane separating the two cells. Ratios were obtained by dividing both elliptical regions by the signal intensity at the plasma membrane (obtaining the “dividing ratio” for the dividing cell and the “non-dividing ratio” for the non-dividing cell). Finally, the ratio between the “dividing ratio” and the “non-dividing ratio” was analyzed. Final ratios equal to 1 indicated that there was no enrichment during cell division. Final ratio greater than 1 indicated an enrichment during cell division at the phragmoplast. Final ratio less than 1 indicated a depletion during cell division at the phragmoplast. This index was performed on the young dividing cells where the cell plate is expanding and not attached and in old dividing cells where the cell plate is partially attached to the plasma membrane (discontinuous phragmoplast).

PI4P accumulation index on the cell plate: The intensity of 2xmCherry2xPH^{FAPP1} signals was quantified on the cell plate at the final cell plate expansion (late ring or discontinuous phragmoplast). Two ROI were design, one on the entire cell plate, the other on the apical plasma membrane. Measured intensity

at the cell plate were then normalized (divided) by the measured intensity at the plasma membrane of the same cell as describe in (*18*).

KNOLLE accumulation index on the cell plate: The intensity of YFP-KNOLLE signals was quantified on the cell plate at the final cell plate expansion (late ring or discontinuous phragmoplast). Two ROI were design, one on the entire cell plate, the other on the cytoplasm. Measured intensity at the cell plate were then normalized (divided) by the measured intensity on the cytoplasm of the same cell as describe in (*18*).

Phragmoplast measurements: Phragmoplast width and length were manually measured using ImageJ, "straight line" tool as represented in fig. S10B.

Statistical analysis

We performed all our statistical analyses in R (version 3.5.0 (2018-04-23), using R studio interface and the packages ggplot2 (*55*), lme4 (*56*), car (*57*), multcomp (*58*) and means (*59*). Graphs were obtained with R and R-studio software, and customized with Inkscape (https://inkscape.org).

The number of division defects was compared using a generalized linear model with a Poisson law (when effectives >20 or using a Quasi-Poisson law if under 20).

Fluorescence intensity indexes were compared using an ANOVA statistical test and a Tuckey HSD post hoc analysis if the normality was verified or using a Kruskal-Wallis test, Dunn (Bonferroni method) Post hoc analyses, if not. All the statistics are found in supplemental tables B to N.

REFERENCES

1. A. Smertenko, F. Assaad, F. Baluska, M. Bezanilla, H. Buschmann, G. Drakakaki, M. T. Hauser, M. Janson, Y. Mineyuki, I. Moore, S. Muller, T. Murata, M. S. Otegui, E. Panteris, C. Rasmussen, A. C. Schmit, J. Samaj, L. Samuels, L. A. Staehelin, D. Van Damme, G. Wasteneys, V. Zarsky, Plant Cytokinesis: Terminology for Structures and Processes. *Trends Cell Biol*. **27**, 885–894 (2017).

2. P. Livanos, S. Muller, Division Plane Establishment and Cytokinesis. *Annual review of plant biology*. **70**, 239–267 (2019).

3. J. Chang-Jie, S. Sonobe, Identification and preliminary characterization of a 65 kDa higher-plant microtubule-associated protein. *Journal of Cell Science*. **105**, 891–901 (1993).

4. Y. R. Lee, B. Liu, Identification of a phragmoplast-associated kinesin-related protein in higher plants. *Current biology : CB*. **10**, 797–800 (2000).

5. P. J. Moore, L. A. Staehelin, Immunogold localization of the cell-wall-matrix polysaccharides rhamnogalacturonan I and xyloglucan during cell expansion and cytokinesis inTrifolium pratense L.; implication for secretory pathways. *Planta*. **174**, 433–445 (1988).

6. A. L. Samuels, T. H. Giddings, L. A. Staehelin, Cytokinesis in tobacco BY-2 and root tip cells: a new model of cell plate formation in higher plants. *J Cell Biol*. **130**, 1345–57 (1995).

7. J. M. Segui-Simarro, J. R. Austin, E. A. White, L. A. Staehelin, Electron tomographic analysis of somatic cell plate formation in meristematic cells of Arabidopsis preserved by high-pressure freezing. *The Plant cell*. **16**, 836–56 (2004).

8. K. Rybak, A. Steiner, L. Synek, S. Klaeger, I. Kulich, E. Facher, G. Wanner, B. Kuster, V. Zarsky, S. Persson, F. F. Assaad, Plant cytokinesis is orchestrated by the sequential action of the TRAPPII and exocyst tethering complexes. *Dev Cell*. **29**, 607–20 (2014).

9. L. C. Noack, Y. Jaillais, Functions of Anionic Lipids in Plants. *Annual review of plant biology*. **71**, 71–102 (2020).

10. M. Heilmann, I. Heilmann, Regulators regulated: Different layers of control for plasma membrane phosphoinositides in plants. *Current Opinion in Plant Biology*. **67**, 102218 (2022).

11. M. L. Simon, M. P. Platre, S. Assil, R. van Wijk, W. Y. Chen, J. Chory, M. Dreux, T. Munnik, Y. Jaillais, A multi-colour/multi-affinity marker set to visualize phosphoinositide dynamics in Arabidopsis. *Plant J*. **77**, 322–37 (2014).

12. A. Lebecq, M. Doumane, A. Fangain, V. Bayle, J. X. Leong, F. Rozier, M. del Marques-Bueno, L. Armengot, R. Boisseau, M. L. Simon, The Arabidopsis SAC9 enzyme is enriched in a cortical population of early endosomes and restricts PI (4, 5) P2 at the plasma membrane. *Elife*. **11**, e73837 (2022).

13. P. Marhava, A. C. Aliaga Fandino, S. W. H. Koh, A. Jelinkova, M. Kolb, D. P. Janacek, A. S. Breda, P. Cattaneo, U. Z. Hammes, J. Petrasek, C. S. Hardtke, Plasma Membrane Domain Patterning and Self-Reinforcing Polarity in Arabidopsis. *Developmental cell*. **52**, 223-235 e5 (2020).

14. Y. Mei, W.-J. Jia, Y.-J. Chu, H.-W. Xue, Arabidopsis phosphatidylinositol monophosphate 5-kinase 2 is involved in root gravitropism through regulation of polar auxin transport by affecting the cycling of PIN proteins. *Cell research*. **22**, 581–597 (2012).

15. P. Scholz, J. Anstatt, H. E. Krawczyk, T. Ischebeck, Signalling pinpointed to the tip: the complex regulatory network that allows pollen tube growth. *Plants*. **9**, 1098 (2020).

16. M. Doumane, A. Lebecq, L. Colin, A. Fangain, F. D. Stevens, J. Bareille, O. Hamant, Y. Belkhadir, T. Munnik, Y. Jaillais, M.-C. Caillaud, Inducible depletion of PI(4,5)P2 by the synthetic iDePP system in Arabidopsis. *Nature Plants*. **7**, 587–597 (2021).

17. M. Fratini, P. Krishnamoorthy, I. Stenzel, M. Riechmann, M. Matzner, K. Bacia, M. Heilmann, I. Heilmann, Plasma membrane nano-organization specifies phosphoinositide effects on Rho-GTPases and actin dynamics in tobacco pollen tubes. *The Plant Cell*. **33**, 642–670 (2021).

18. F. Lin, P. Krishnamoorthy, V. Schubert, G. Hause, M. Heilmann, I. Heilmann, A dual role for cell plate-associated PI4Kbeta in endocytosis and phragmoplast dynamics during plant somatic cytokinesis. *The EMBO journal*. **38** (2019), doi:10.15252/embj.2018100303.

19. M. L. Simon, M. P. Platre, M. M. Marques-Bueno, L. Armengot, T. Stanislas, V. Bayle, M. C. Caillaud, Y. Jaillais, A PtdIns(4)P-driven electrostatic field controls cell membrane identity and signalling in plants. *Nat Plants*. **2**, 16089 (2016).

20. W. Van Leeuwen, J. E. Vermeer, T. W. Gadella Jr, T. Munnik, Visualization of phosphatidylinositol 4, 5-bisphosphate in the plasma membrane of suspension-cultured tobacco BY-2 cells and whole Arabidopsis seedlings. *The Plant Journal*. **52**, 1014–1026 (2007).

21. M. Doumane, A. Lebecq, A. Fangain, V. Bayle, F. Rozier, M. del M. Marquès-Bueno, R. P. Boisseau, M. L. A. Simon, L. Armengot, Y. Jaillais, M.-C. Caillaud, *bioRxiv*, in press, doi:10.1101/2021.09.10.459735.

22. S. Muller, A. Smertenko, V. Wagner, M. Heinrich, P. J. Hussey, M. T. Hauser, The plant microtubule-associated protein AtMAP65-3/PLE is essential for cytokinetic phragmoplast function. *Current biology : CB*. **14**, 412–7 (2004).

23. K. L. Farquharson, MAP65-3 cross-links interdigitated microtubules in the phragmoplast. *The Plant cell*. **23**, 2807 (2011).

24. C. M. Ho, T. Hotta, F. Guo, R. W. Roberson, Y. R. Lee, B. Liu, Interaction of antiparallel microtubules in the phragmoplast is mediated by the microtubule-associated protein MAP65-3 in Arabidopsis. *The Plant cell*. **23**, 2909–23 (2011).

25. C. M. Ho, Y. R. Lee, L. D. Kiyama, S. P. Dinesh-Kumar, B. Liu, Arabidopsis microtubule-associated protein MAP65-3 cross-links antiparallel microtubules toward their plus ends in the phragmoplast via its distinct C-terminal microtubule binding domain. *The Plant cell*. **24**, 2071–85 (2012).

26. M. Sasabe, K. Kosetsu, M. Hidaka, A. Murase, Y. Machida, Arabidopsis thaliana MAP65-1 and MAP65-2 function redundantly with MAP65-3/PLEIADE in cytokinesis downstream of MPK4. *Plant signaling & behavior*. **6**, 743–7 (2011).

27. M. Beck, G. Komis, A. Ziemann, D. Menzel, J. Samaj, Mitogen-activated protein kinase 4 is involved in the regulation of mitotic and cytokinetic microtubule transitions in Arabidopsis thaliana. *The New phytologist*. **189**, 1069–83 (2011).

28. M. C. Caillaud, P. Lecomte, F. Jammes, M. Quentin, S. Pagnotta, E. Andrio, J. de Almeida Engler, N. Marfaing, P. Gounon, P. Abad, B. Favery, MAP65-3 microtubule-associated protein is essential for nematode-induced giant cell ontogenesis in Arabidopsis. *The Plant cell*. **20**, 423–37 (2008).

29. S. Berriri, A. V. Garcia, N. F. dit Frey, W. Rozhon, S. Pateyron, N. Leonhardt, J.-L. Montillet, J. Leung, H. Hirt, J. Colcombet, Constitutively Active Mitogen-Activated Protein Kinase Versions Reveal Functions of Arabidopsis MPK4 in Pathogen Defense Signaling. *The Plant Cell*. **24**, 4281–4293 (2012).

30. E. Jaber, K. Thiele, V. Kindzierski, C. Loderer, K. Rybak, G. Jurgens, U. Mayer, R. Sollner, G. Wanner, F. F. Assaad, A putative TRAPPII tethering factor is required for cell plate assembly during cytokinesis in Arabidopsis. *New Phytol*. **187**, 751–63 (2010).

31. M. Thellmann, K. Rybak, K. Thiele, G. Wanner, F. F. Assaad, Tethering factors required for cytokinesis in Arabidopsis. *Plant physiology*. **154**, 720–32 (2010).

32. A. Steiner, L. Muller, K. Rybak, V. Vodermaier, E. Facher, M. Thellmann, R. Ravikumar, G. Wanner, M. T. Hauser, F. F. Assaad, The Membrane-Associated Sec1/Munc18 KEULE is Required for Phragmoplast Microtubule Reorganization During Cytokinesis in Arabidopsis. *Mol Plant*. **9**, 528–40 (2016).

33. H. Li, B. Sun, M. Sasabe, X. Deng, Y. Machida, H. Lin, Y.-R. Julie Lee, B. Liu, Arabidopsis MAP 65-4 plays a role in phragmoplast microtubule organization and marks the cortical cell division site. *New Phytologist*. **215**, 187–201 (2017).

34. M. Doumane, C. Lionnet, V. Bayle, Y. Jaillais, M. C. Caillaud, Automated Tracking of Root for Confocal Time-lapse Imaging of Cellular Processes. *Bio Protoc*. **7** (2017), doi:10.21769/BioProtoc.2245.

35. S. Muller, S. Han, L. G. Smith, Two kinesins are involved in the spatial control of cytokinesis in Arabidopsis thaliana. *Current biology : CB*. **16**, 888–94 (2006).

36. M. C. Caillaud, Anionic Lipids: A Pipeline Connecting Key Players of Plant Cell Division. *Frontiers in plant science*. **10**, 419 (2019).

37. E. P. Eleftheriou, T. I. Baskin, P. K. Hepler, Aberrant cell plate formation in the Arabidopsis thaliana microtubule organization 1 mutant. *Plant & cell physiology*. **46**, 671–5 (2005).

38. K. L. Walker, S. Muller, D. Moss, D. W. Ehrhardt, L. G. Smith, Arabidopsis TANGLED identifies the division plane throughout mitosis and cytokinesis. *Current biology : CB*. **17**, 1827–36 (2007).

39. D. Stockle, A. Herrmann, E. Lipka, T. Lauster, R. Gavidia, S. Zimmermann, S. Muller, Putative RopGAPs impact division plane selection and interact with kinesin-12 POK1. *Nat Plants*. **2**, 16120 (2016).

40. D. Dambournet, M. Machicoane, L. Chesneau, M. Sachse, M. Rocancourt, A. El Marjou, E. Formstecher, R. Salomon, B. Goud, A. Echard, Rab35 GTPase and OCRL

phosphatase remodel lipids and F-actin for successful cytokinesis. *Nature cell biology*. **13**, 981–8 (2011).

41. A. Echard, Phosphoinositides and cytokinesis: the “PIP” of the iceberg. *Cytoskeleton*. **69**, 893–912 (2012).

42. A. H. Vollmer, N. N. Youssef, D. B. DeWald, Unique cell wall abnormalities in the putative phosphoinositide phosphatase mutant AtSAC9. *Planta*. **234**, 993–1005 (2011).

43. F. F. Assaad, U. Mayer, G. Wanner, G. Jurgens, The KEULE gene is involved in cytokinesis in Arabidopsis. *Molecular & general genetics : MGG*. **253**, 267–77 (1996).

44. W. Lukowitz, U. Mayer, G. Jurgens, Cytokinesis in the Arabidopsis embryo involves the syntaxin-related KNOLLE gene product. *Cell*. **84**, 61–71 (1996).

45. M. H. Lauber, I. Waizenegger, T. Steinmann, H. Schwarz, U. Mayer, I. Hwang, W. Lukowitz, G. Jurgens, The Arabidopsis KNOLLE protein is a cytokinesis-specific syntaxin. *J Cell Biol*. **139**, 1485–93 (1997).

46. I. Waizenegger, W. Lukowitz, F. Assaad, H. Schwarz, G. Jurgens, U. Mayer, The Arabidopsis KNOLLE and KEULE genes interact to promote vesicle fusion during cytokinesis. *Current biology : CB*. **10**, 1371–4 (2000).

47. S. Muller, G. Jurgens, Plant cytokinesis-No ring, no constriction but centrifugal construction of the partitioning membrane. *Seminars in cell & developmental biology*. **53**, 10–8 (2016).

48. D. Van Damme, S. Coutuer, R. De Rycke, F. Y. Bouget, D. Inze, D. Geelen, Somatic cytokinesis and pollen maturation in Arabidopsis depend on TPLATE, which has domains similar to coat proteins. *The Plant cell*. **18**, 3502–18 (2006).

49. M. Karimi, A. Depicker, P. Hilson, Recombinational cloning with plant gateway vectors. *Plant physiology*. **145**, 1144–54 (2007).

50. N. C. Shaner, R. E. Campbell, P. A. Steinbach, B. N. Giepmans, A. E. Palmer, R. Y. Tsien, Improved monomeric red, orange and yellow fluorescent proteins derived from Discosoma sp. red fluorescent protein. *Nature biotechnology*. **22**, 1567–1572 (2004).

51. S. J. Clough, A. F. Bent, Floral dip: a simplified method for Agrobacterium-mediated transformation of Arabidopsis thaliana. *The Plant Journal*. **16**, 735–743 (1998).

52. K. Belcram, D. Legland, M. Pastuglia, "Quantification of Cell Division Angles in the Arabidopsis Root" in *Plant Cell Division* (Springer, 2022), pp. 209–221.

53. M. Romeiro Motta, X. Zhao, M. Pastuglia, K. Belcram, F. Roodbarkelari, M. Komaki, H. Harashima, S. Komaki, M. Kumar, P. Bulankova, B1-type cyclins control microtubule organization during cell division in Arabidopsis. *EMBO reports*. **23**, e53995 (2022).

54. D. Legland, I. Arganda-Carreras, P. Andrey, MorphoLibJ: integrated library and plugins for mathematical morphology with ImageJ. *Bioinformatics*. **32**, 3532–3534 (2016).

55. H. Wickham, *ggplot2: elegant graphics for data analysis* (springer, 2016).

56. D. Bates, M. Mächler, B. Bolker, S. Walker, Fitting Linear Mixed-Effects Models Using lme4. *J. Stat. Soft.* **67**, 1–48 (2015).

57. J. Fox, S. Weisberg, The car package contains functions and data sets associated with the book an R companion to applied regression. R-Project (2011).

58. F. Bretz, T. Hothorn, P. Westfall, *Multiple comparisons using R* (CRC press, 2016).

59. R. Lenth, M. R. Lenth, Package 'lsmeans.' *The American Statistician*. **34**, 216–221 (2018).

ACKNOWLEDGEMENTS

We are grateful to the SiCE group in particular Yvon Jaillais and Vincent Bayle for comments and discussions, as well as Charlotte Kirchhelle, Liam Elliot, Olivier Hamant (RDP, ENS de Lyon, France) for their great input on the manuscript. We thank Patrice Bolland, Alexis Lacroix from our plant facility, Claire Lionnet and Vincent Bayle for microscopy advice. We acknowledge the contribution of SFR Biosciences (UMS3444/CNRS, US8/Inserm, ENS de Lyon, UCBL) facilities at the LBI-PLATIM-MICROSCOPY for assistance with imaging. We are grateful to Bruno Favery (INRAe Sophia Antipolis) for sharing MAP65-3 material with use. We thank G. Jürgens, (University of Tübingen, Germany) for the anti-KNOLLE antibody and J. Colcombet (IPS2 - Université Paris-Saclay) for the MPK4 related material.

FUNDINGS

This work was supported by Seed Fund ENS LYON; ANR-16-CE13-0021 to MCC and ANR-20-CE13-0026-02 to MCC and DB. AL is funded by Ph.D. fellowships from the French Ministry of Research and Higher Education. CG is funded by EMBO fellowship ATLF 646-2021(European Molecular Biology Organization, Heidelberg, DE) and ANR-20-CE13-0026-02.

AUTHOR CONTRIBUTIONS

Conceptualization: AL, MCC

Methodology: AL, KB, AF, EG, CG

Investigation: AL, EG, MCC, CG

Visualization: AL, CG

Supervision: MCC, MP, DB

Writing – original draft: AL, MCC

Writing – review & editing: AL, MCC, MP, DB

COMPETING INTERESTS

Authors declare that they have no competing interests.

DATA AND MATERIALS AVAILABILITY

All data needed to evaluate the conclusions in the paper are present in the paper and/or the Supplementary Materials.

FIGURES

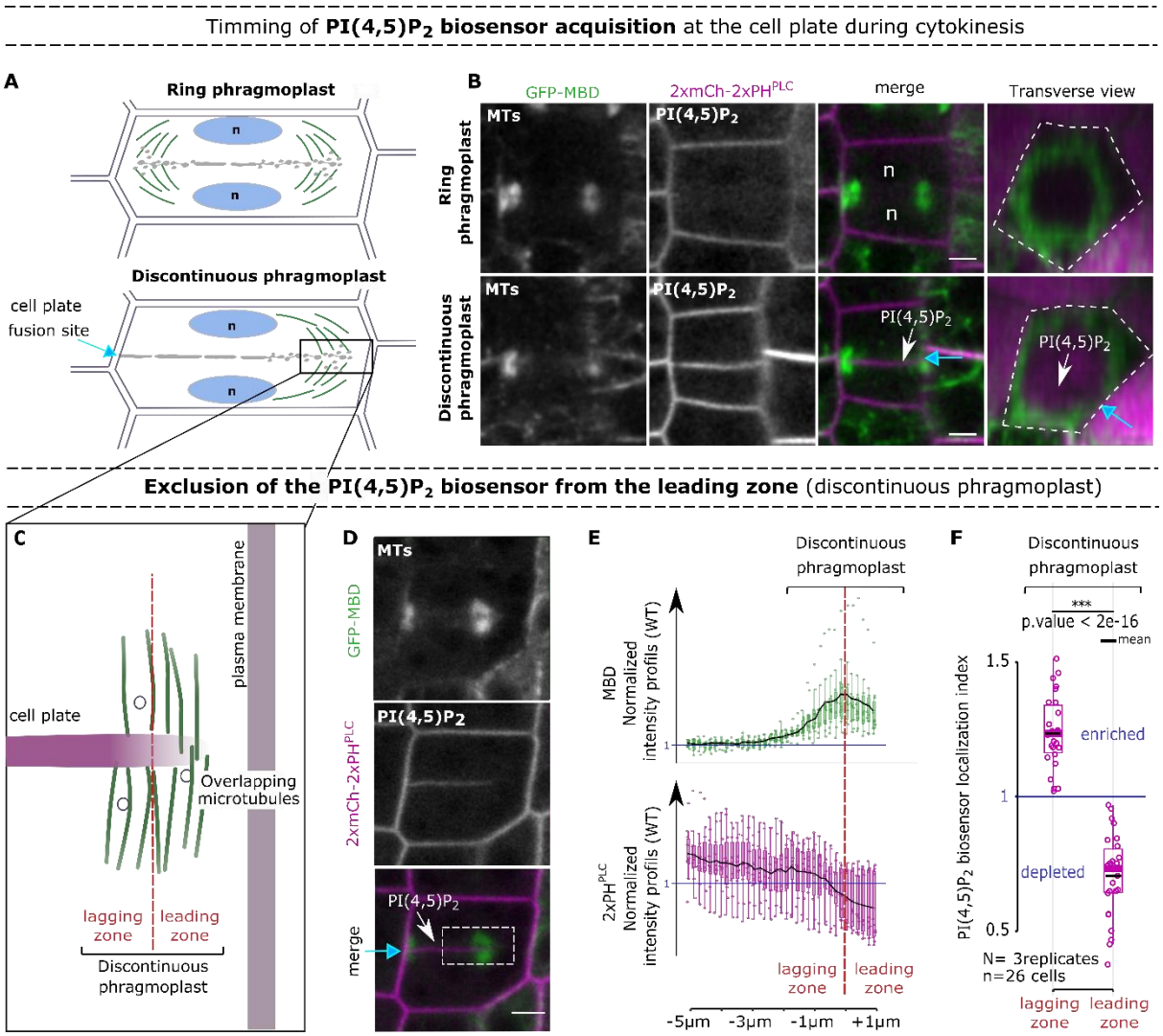

Fig.1 | <u>PI(4,5)P_2 is recruited at the cell plate after its unilateral attachment.</u>
A, Representation of the unattached cell plate showing a ring phragmoplast (top) and the unilaterally attached cell plate corresponding to a discontinuous phragmoplast (bottom). **B**, Confocal images with a root tracking system (*34*) of 2xmCh-2xPH^{PLC} with the microtubule reporter line GFP-MBD during the two steps represented in (A). Single longitudinal sections for each fluorescent channel and a transverse section of the merge channels is presented (0.7µm between optical sections). Dotted line, cell contour. **C**, Representation of the expanding edge of a discontinuous phragmoplast. **D**, Images of 2xmCh-2xPH^{PLC} and GFP-MBD at the unilaterally attached cell plate. **E**, Normalized intensity profiles at 6 µm along the discontinuous phragmoplast (ROI). **F**, PI(4,5)P_2 biosensor localization index (normalized by the cell plate intensity) on the phragmoplast lagging/leading zones. In the plots, middle horizontal bars represent the median, while the bottom and top of each box represent the 25th and 75th percentiles, respectively. At most, the whiskers extend to 1.5 times the interquartile range, excluding data beyond. For range of value under 1,5 IQR, whiskers represent the range of maximum and minimum values. Results of the statistical analysis (shown in the supplementary table) are presented (N = number of replicates, n = number of cells). White arrow, PI(4,5)P_2 biosensor appearance; Blue arrow, cell plate fusion site; red dotted line, separation leading and lagging zone; dotted lines, region of interest; n, nucleus; scale bars, 5 µm.

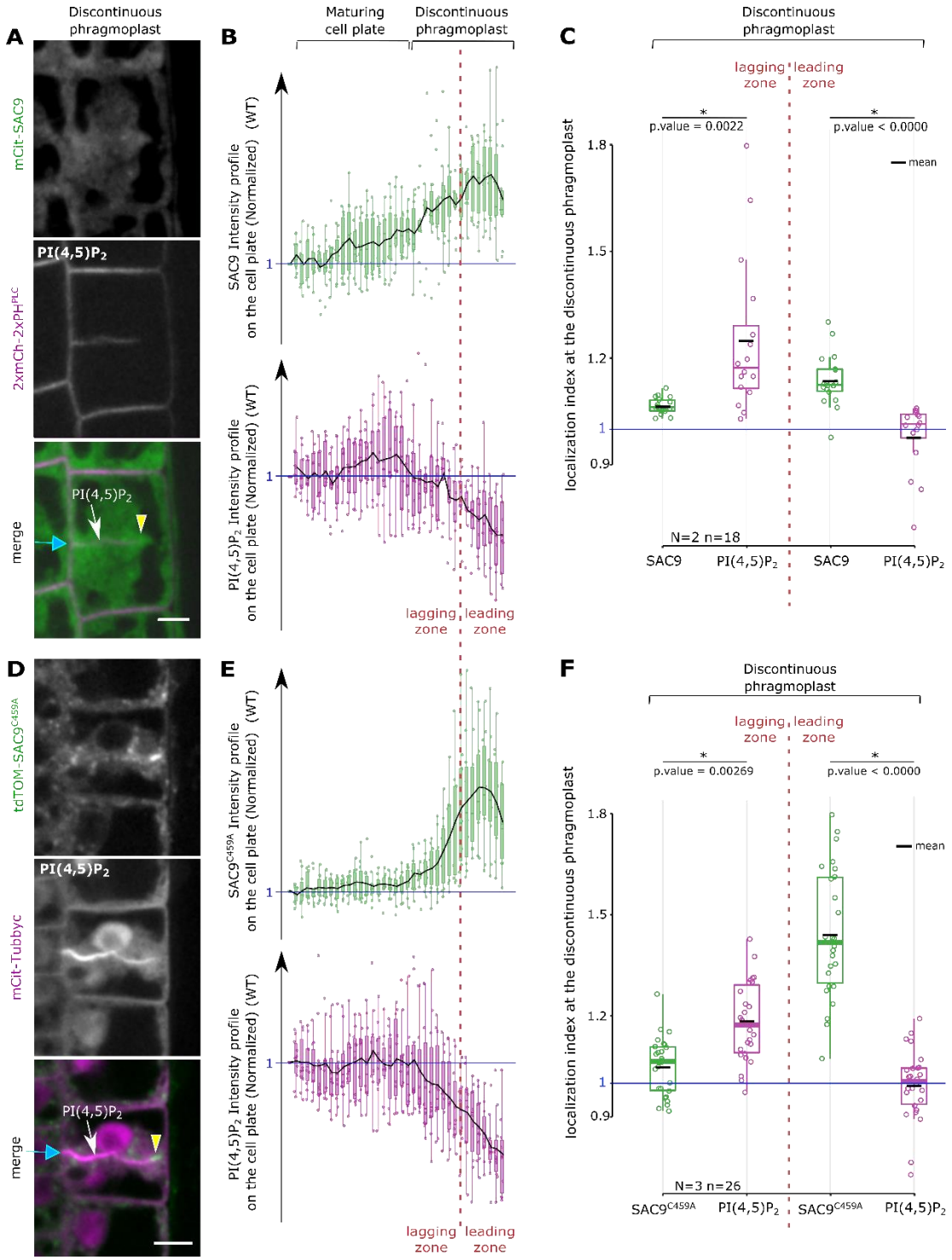

Fig.2 | SAC9 and the PI(4,5)P_2 are mutually co-excluded at the cell plate.
A, Images of mCit-SAC9 with 2xmCh-2xPH^{PLC} when the cell plate is unilaterally attached. **B**, Normalized intensity profiles corresponding to (a). **C**, Quantification of the localization index corresponding to (A). **D**, Images of tdTOM-SAC9^{C459A} with mCit-Tubbyc when the cell plate is unilaterally attached. **E**, Normalized intensity profiles corresponding to (d). **F**, Quantification of the localization index corresponding to (D). Blue arrow, cell plate fusion site; yellow arrowhead, SAC9 enrichment; red dotted line, separation leading and lagging zone; n, nucleus; scale bar, 5µm.

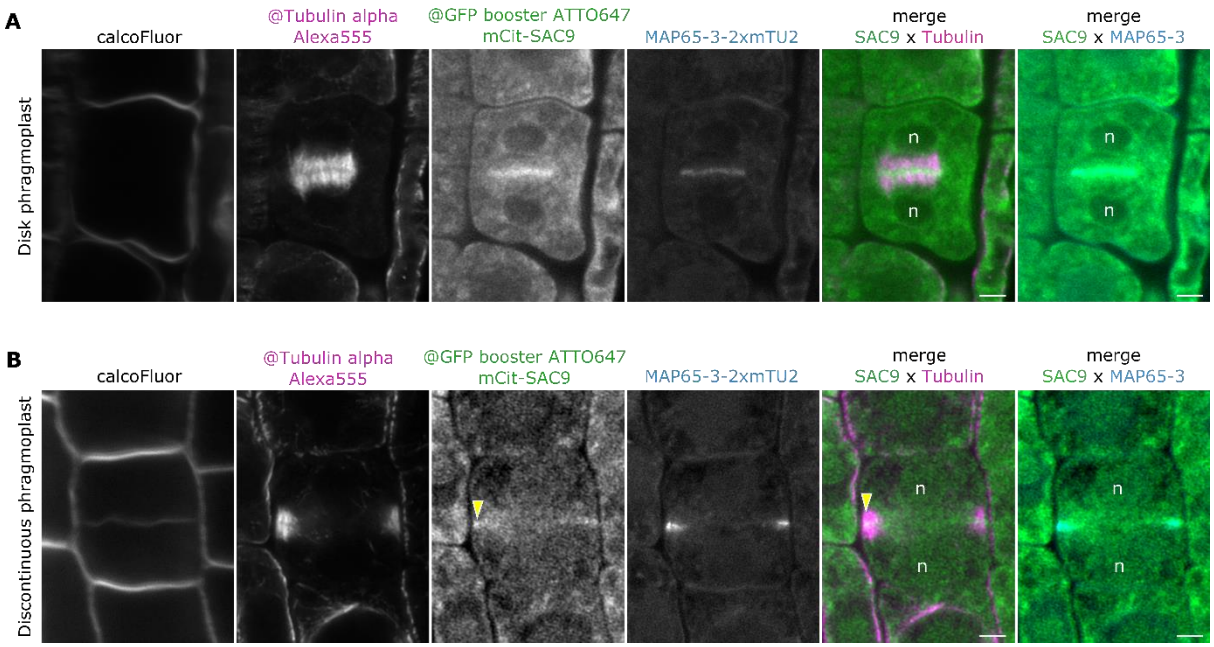

Fig.3| Super resolution microscopy reveals the colocalization of SAC9 with MAP65-3 at the leading edges of the cell plate.

A, **B**, from left to right: cell wall marker, calcofluor, Super-resolution microtubules revealed with @tubulin alpha antibodies (alexa555 secondary antibodies) with mCit-SAC9 revealed by GFP-booster ATTO647 antibody accompanied by MAP65-3-2xmTU2 preserved fluorescence. Two phragmoplast stages are presented: the disk phragmoplast (A) and discontinuous phragmoplast (B).

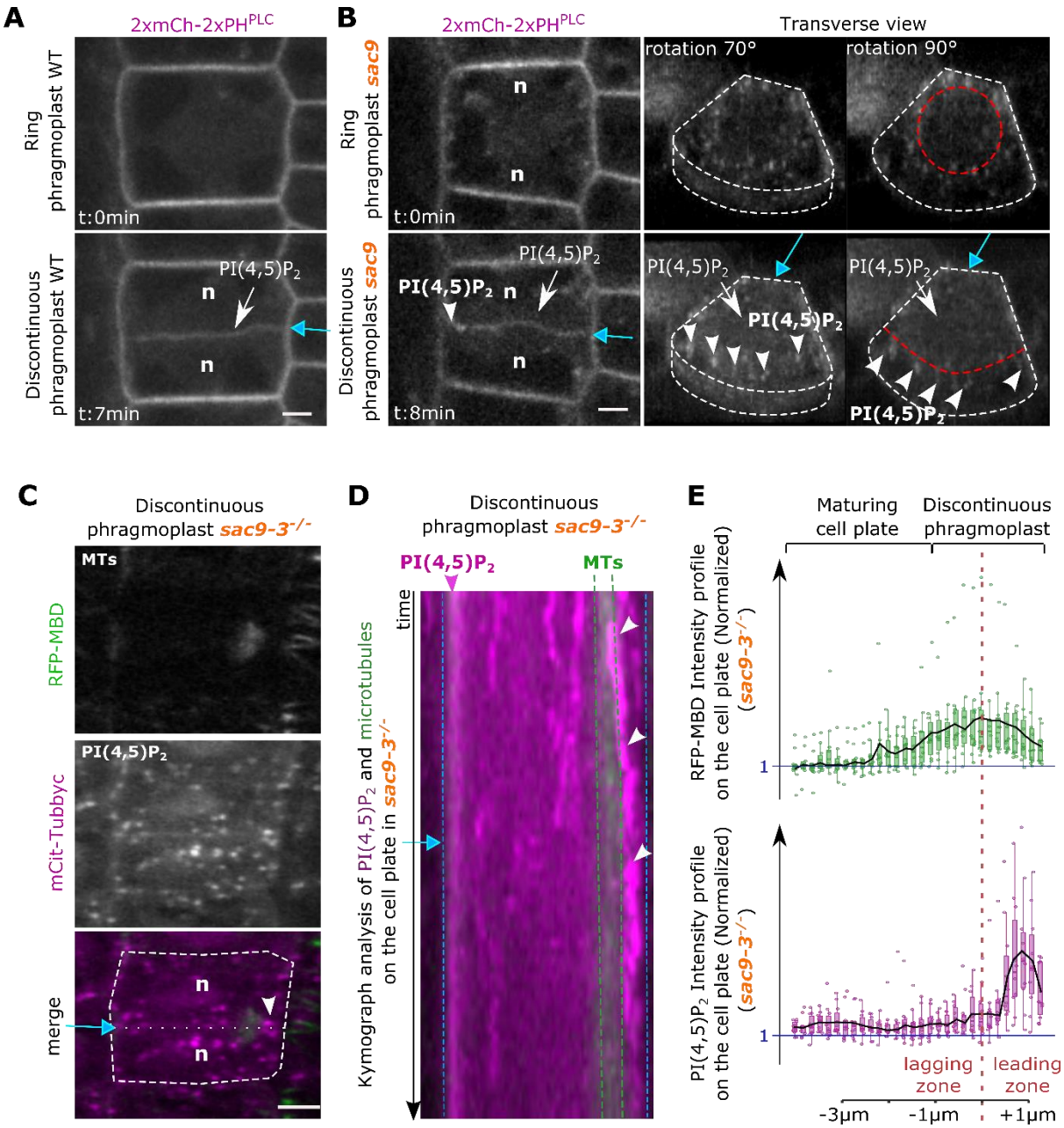

Fig.4| In *sac9-3*, PI(4,5)P_2 pool precedes the phragmoplast leading edge during late cytokinesis.

A, Images extracted from a time-lapse imaging in WT of 2xmCh-2xPH^{PLC} at two cytokinetic steps: ring (upper panel) and discontinuous (lower panel) phragmoplast stages. **B**, Images extracted from a time-lapse imaging in *sac9-3* of 2xmCh-2xPH^{PLC} at two cytokinetic steps: ring (upper panel) and discontinuous (lower panel) phragmoplast stages. On the right panel are presented two transverse view of 2xmCh-2xPH^{PLC} for both stages in *sac9-3* (0.3 µm between optical sections). **C**, Images of mCit-Tubbyc with RFP-MBD in *sac9-3*. **D**, Kymograph representation of PI(4,5)P_2 and MTs at the cell plate during the discontinuous phase in *sac9-3* (related to panel c). Image were taken every 5 seconds for a total duration of 5 minutes. **E**, Normalized intensity profiles corresponding to (C). White arrow, PI(4,5)P_2 biosensor appearance; White arrowhead, abnormal PI4,5)P_2 enrichment at the leading zone in *sac9-3*; purple arrowhead: PI(4,5)P_2 biosensor continuous enrichment at the cell plate-plasma membrane junction; White dotted line, cell contour; Red dotted line, separation leading and lagging zone; Green dotted line: delimitation of the phragmoplast; Blue arrow, cell plate fusion site; n, nucleus; Scale bars, 5µm.

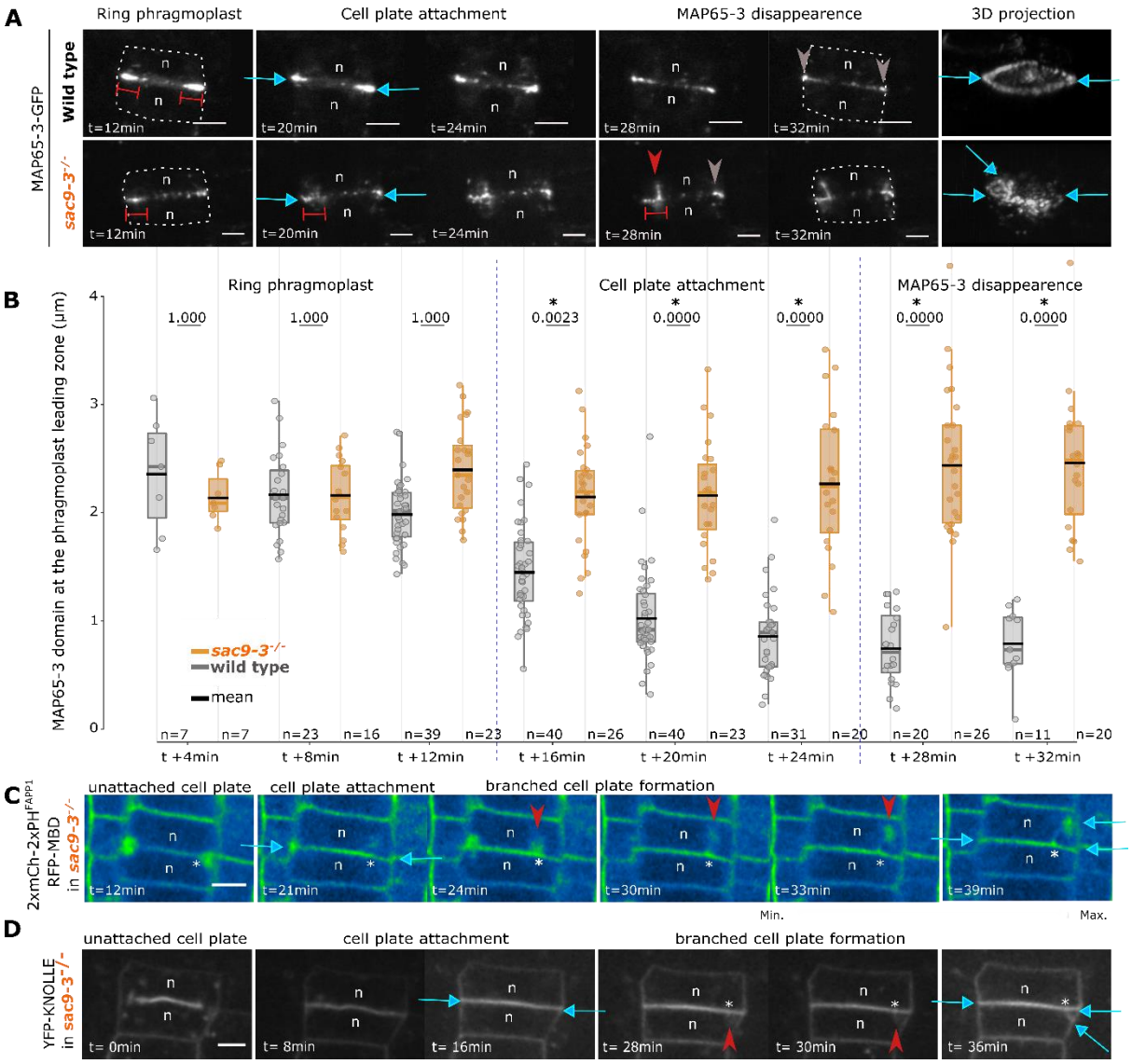

Fig.5 | *de-novo* recruitment of the cytokinesis apparatus in *sac9-3*

A, Image series of MAP65-3-GFP in WT (upper panel) or *sac9-3* (of the bottom panel) every two minutes for two hours. Time is given relative to "disk"-"ring" phragmoplast transition (0 min) and cell plate attachment (14 min). Finals images represent a 3D view of time = 32 min. **B**, Comparison of MAP65-3-GFP domain length in WT versus *sac9-3*. In the plots, middle horizontal bars represent the median, while the bottom and top of each box represent the 25th and 75th percentiles, respectively. At most, the whiskers extend to 1.5 times the interquartile range, excluding data beyond. For range of value under 1,5 IQR, whiskers represent the range of maximum and minimum values. Results of the statistical analysis (shown in the supplementary table) are presented (n=number of cells). **C**, Z projection of 2xmCherry-2xPH^{FAPP1} and RFP-MBD in *sac9-3* over time. Here, the signal is color coded in green fire blue (see scale bar on the right). The signal corresponding to microtubules and the one corresponding to membrane are not distinguished). Note that here, 2xmCh-2xPH^{FAPP1} is used at the membrane marker (plasma membrane and cell plate). **D**, Image series of YFP-KNOLLE in *sac9-3*. Gray arrow, MAP65-3 localization after cytokinesis; Double red bars, distance labeled by GFP-MAP65-3; red arrowhead, branch emergence in *sac9-3*; blue arrow, cell plate fusion site; Asterisk, position of the branch's emergence at the cell plate; n, nucleus; scale bars, 5µm.

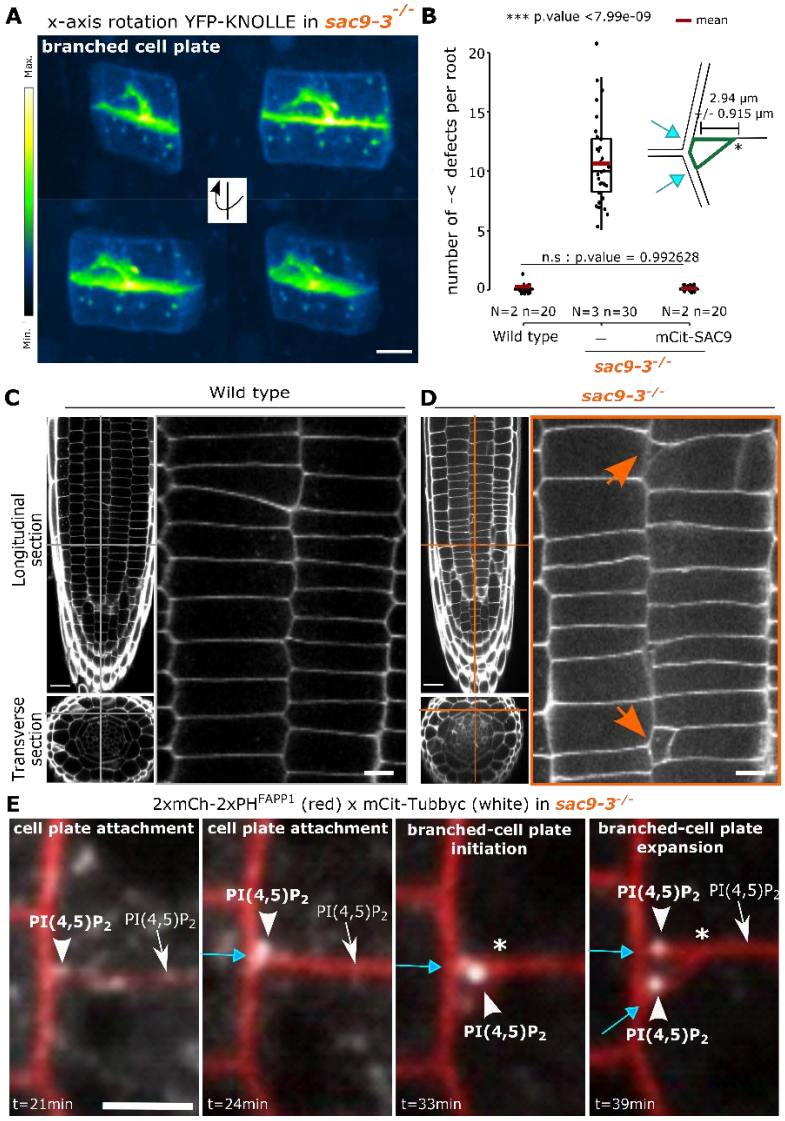

Fig.6 | Ectopic membrane domain formed in absence of SAC9 has a cell plate identity and leads to cell wall defects.

A, 3D rotation of YFP-KNOLLE in *sac9-3* during defective cytokinesis. Here, the signal is color coded in green fire blue (see scale bar). Scale bars, 5µm. **B**, Quantification of the number of defects. The result of the statistical analysis (shown in the supplementary table) is presented. On the top right, representation of branched cell wall defects (green) with key topological elements listed such as the distance between the branched cell wall and lateral cell wall (double arrow), and cell plate insertion site (blue arrow). In the plots, middle horizontal bars represent the median, while the bottom and top of each box represent the 25th and 75th percentiles, respectively. At most, the whiskers extend to 1.5 times the interquartile range, excluding data beyond. For range of value under 1,5 IQR, whiskers represent the range of maximum and minimum values. Results of the statistical analysis (shown in the supplementary table) are presented (N = number of replicates, n = number of cells). **C-D**, Z-stack images of calcofluor-stained fixed roots (7 day-olds) for WT (C) and *sac9-3* (D). Orange lines, the position of the section. Left panel, longitudinal section (top, scale bars 20 µm), and transverse section (bottom). Right panel, a crop of the root cortex (scale bars 5 µm). **e**, Time series of mCit-Tubbyc and 2mCh-2PH^{FAPP1} at the end of the cytokinesis in *sac9-3* (Bars 5µm). Here, 2xmCh-2xPH^{FAPP1} is used as a marker for membranes (plasma membrane and cell plate). n, nucleus; White asterisk, position of the branch's emergence at the cell plate; Orange arrow, cell wall defects; Blue arrow, cell plate fusion site; White arrowhead, PI(4,5)P_2 biosensor enrichment observed in *sac9-3*. Scale bars, 5µm.

SUPPLEMENTARY FIGURES

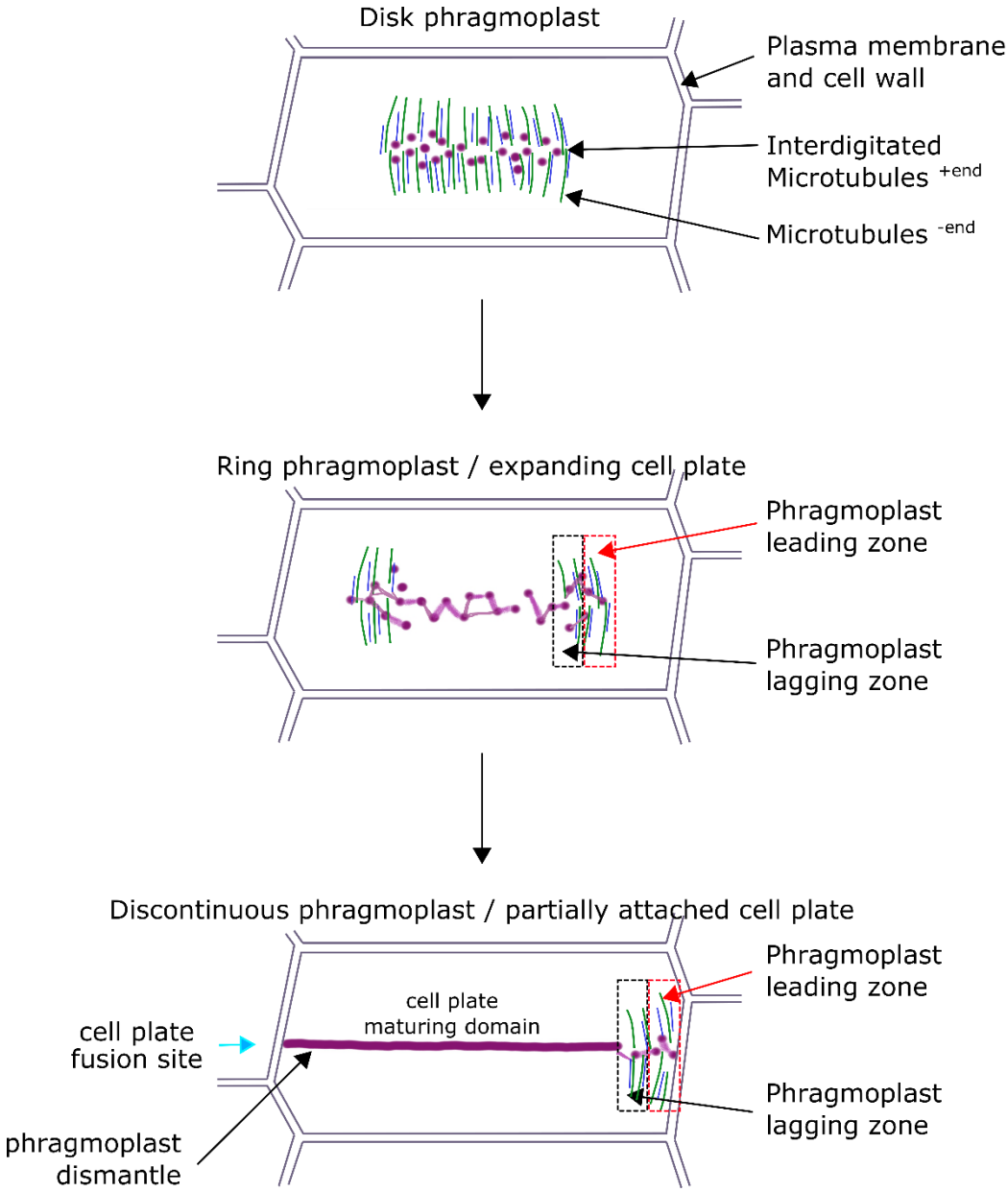

Fig. S1 | Cell cytokinesis from a cytoskeleton point of view.

Schematic representation of phragmoplast expansion in a 2D cell. The three main phragmoplast structures are presented: form a Disk phragmoplast until a Discontinuous phragmoplast morphology. Key cytoskeleton's structures are presented: Microtubules plus ends, minus ends, phragmoplast leading and lagging zones and cell plate maturing domain. Microtubules, green; Actin, blue, Cell plate, magenta.

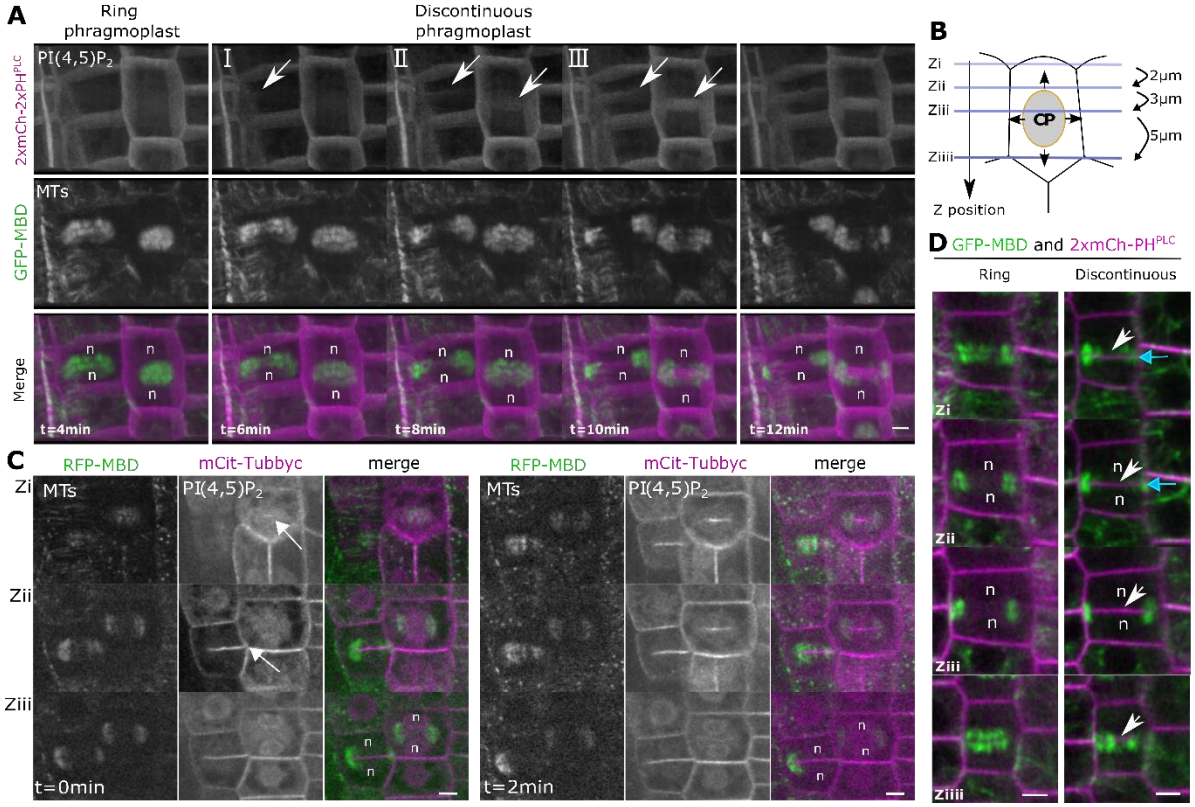

Fig. S2 | PI(4,5)P_2 appearance at the maturing cell plate in wild-type plants

A, Z-projection of dividing cells expressing 2xmCh-2xPH^{PLC} together with GFP-MBD. The image was taken every 2 min and 15 optical sections were used for Z-projection. I, II and III images correspond to the sequence of events from the first appearance of PI(4,5)P_2 biosensor at the cell plate. **B**, Representation of the different focal planes used in this study from the subcortical part of the cells (Zi, top panel) to the bottom cells (Ziiii, bottom panel). CP, cell plate **C**, Confocal images of WT at different Z, expressing *mCit-Tubbyc* together with RFP-*MBD* during the discontinuous phragmoplast stage, in wild type plants. **D**, Confocal images of WT, expressing *2xmCh-2xPH^{PLC}* together with *GFP-MBD* during the discontinuous phragmoplast stage, from the subcortical part of the cells (Zi, top panel) to the center of the cells (Ziiii, bottom panel) in WT. White arrow, PI(4,5)P_2 biosensor appearance; blue arrow, cell plate fusion site; Black arrow, cell plate direction of growth; n, nucleus; scale bars, 5µm.

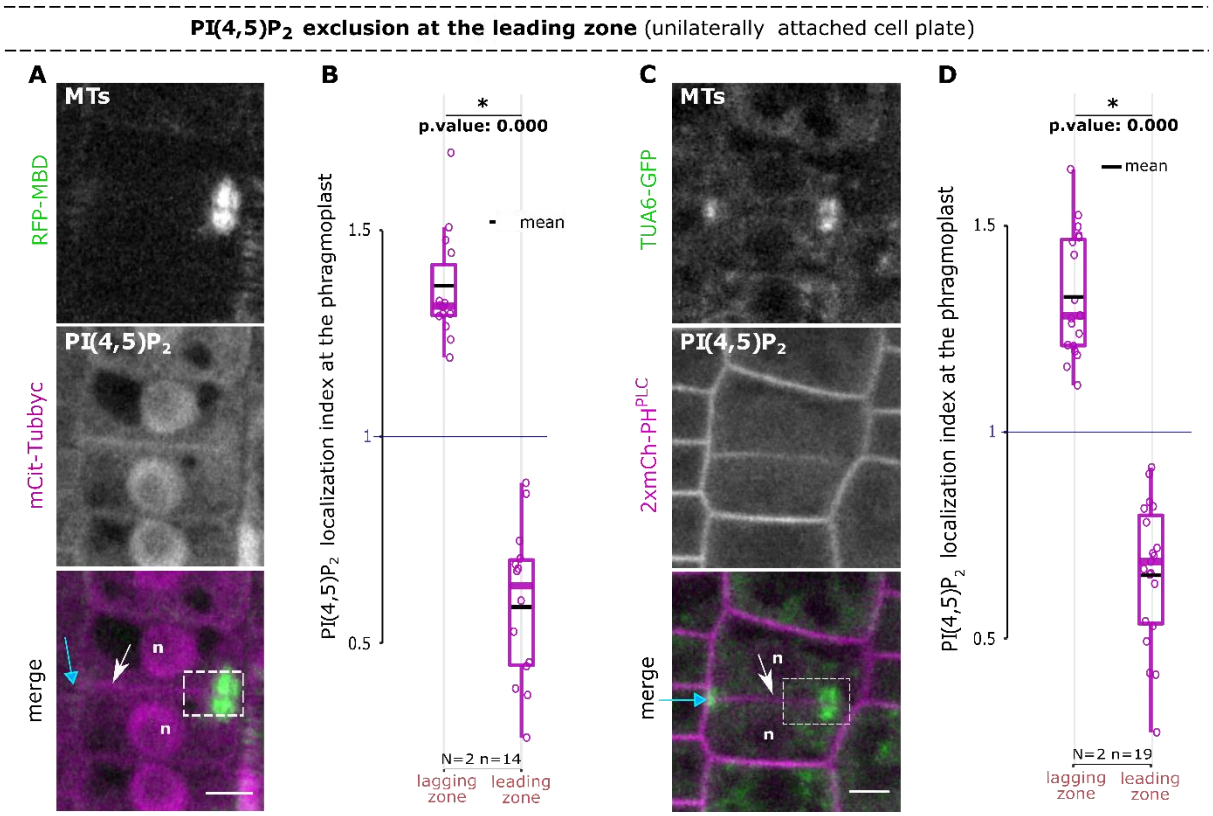

Fig. S3 | PI(4,5)P_2 is absent from the cell plate leading zone in WT

A, C, Confocal images of WT, expressing respectively *mCit-Tubbyc* with *RFP-MBD* (A) or *2xmCh-2xPH*^{PLC} with *TUA6-GFP* (C) at the discontinuous phragmoplast. **B, D**, Quantification of PI(4,5)P_2 localization index for PI(4,5)P_2 biosensors (mCit-Tubbyc and 2xmCh-2xPH^{PLC}) with respect to two microtubules reporter (RFP-MBD or TUA6-GFP respectively), normalized by cell plate intensity. "1" blue line represents a situation in which there is no biosensor enrichment. In the plots, middle horizontal bars represent the median, while the bottom and top of each box represent the 25th and 75th percentiles, respectively. At most, the whiskers extend to 1.5 times the interquartile range, excluding data beyond. For range of value under 1,5 IQR, whiskers represent the range of maximum and minimum values. Results of the statistical analysis (shown in the supplementary table) are presented (N = number of replicates, n = number of cells). White arrow, PI(4,5)P_2 biosensor appearance; Blue arrow, cell plate fusion site; dotted lines, region of interest; n, nucleus; scale bars, 5µm.

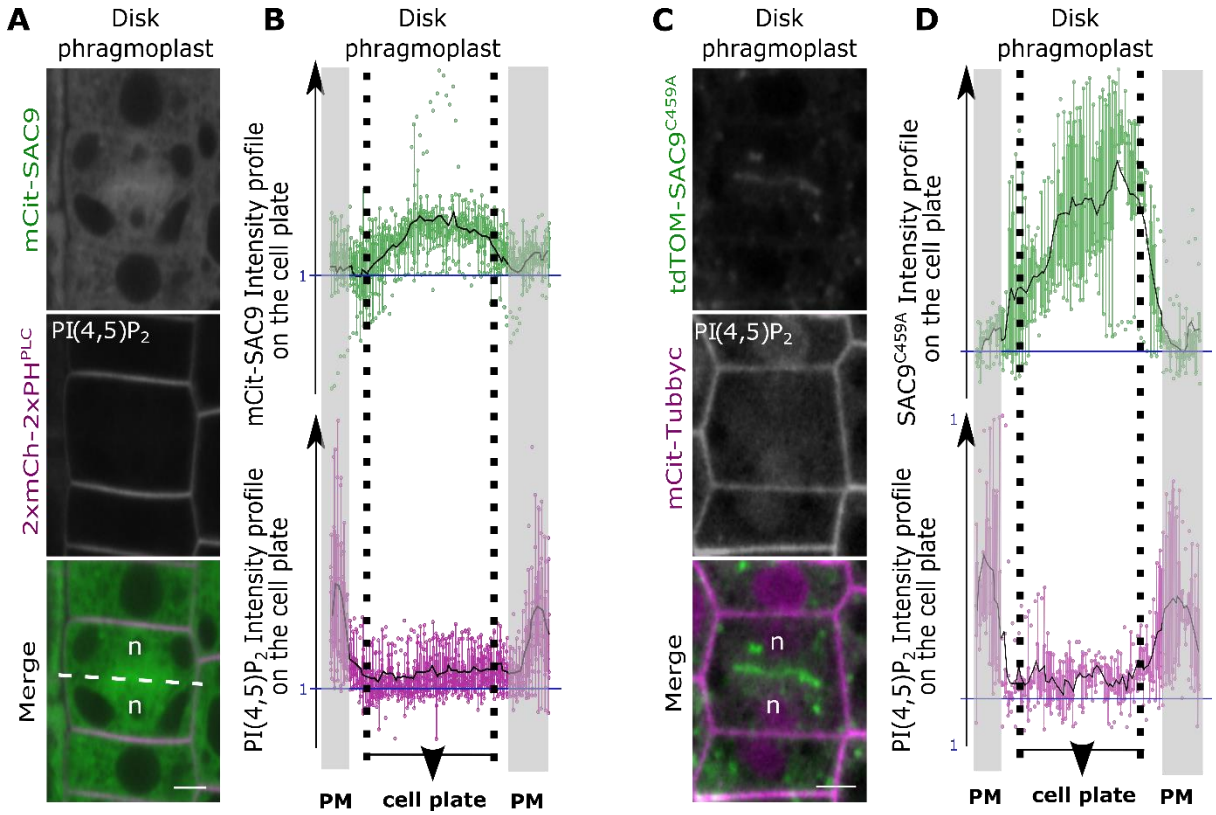

Fig. S4 | SAC9 and the PI(4,5)P_2 localization during the disk phragmoplast stage

A, Confocal images of mCit-SAC9 and 2xmCh-2xPH^{PLC} at the "Disk phragmoplast" phase in WT. **B**, Normalized intensity profiles of mCit-SAC9 (top panel) and 2xmCh-2xPH^{PLC} (bottom panel) during the Disk phragmoplast phase (entire cell plate, dotted line). **C**, Confocal images of WT expressing *tdTOM-SAC9^{C459A}* and *mCit-Tubbyc*. **D**, Normalized intensity profiles of tdTOM-SAC9^{C459A} (top panel) and mCit-Tubbyc (bottom panel).

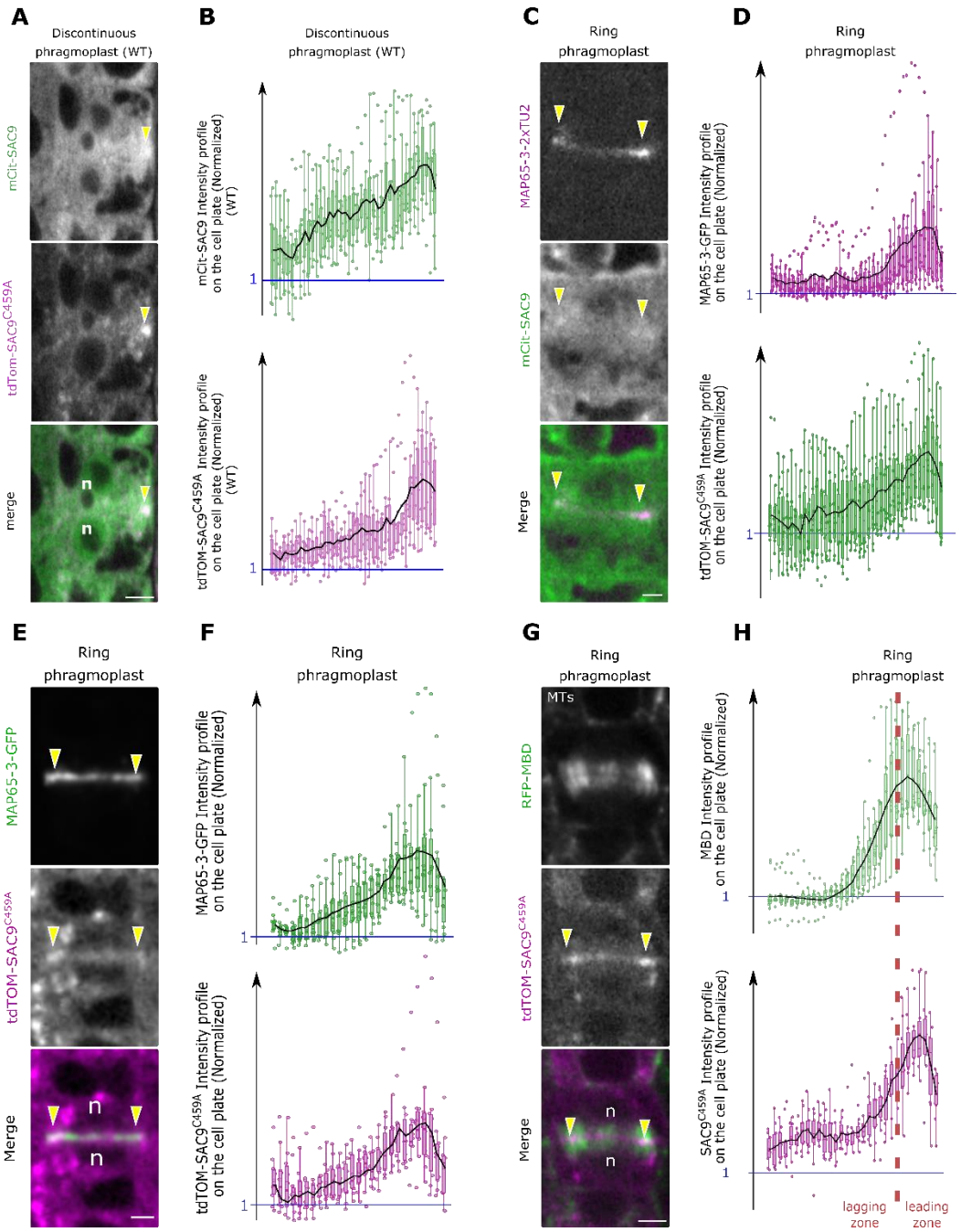

878

879 **Fig. S5 | SAC9 colocalizes with SAC9^{C459A} and MAP65-3 at the phragmoplast leading zone during**
880 **cytokinesis**

881 **A**, Images of mCit-SAC9 with MAP65-3-2xmTU2. **B**, Normalized intensity profiles corresponding to (A).
882 **C**, Images of tdTOM-SAC9^{C459A} with MAP65-3-GFP. **D**, Normalized intensity profiles corresponding to
883 (C). **E**, Images of tdTOM-SAC9^{C459A} and GFP-MBD at the ring phragmoplast stage. **F**, Normalized
884 intensity profiles corresponding to (E). **G**, Images of mCit-SAC9 with tdTOM-SAC9^{C459A} at the
885 discontinuous phragmoplast stage. **H**, Normalized intensity profiles corresponding to (G). Yellow
886 arrowhead, SAC9 and MAP65-3 enrichments at the leading zone; n, nucleus; Scale bar, 5 μm.

887

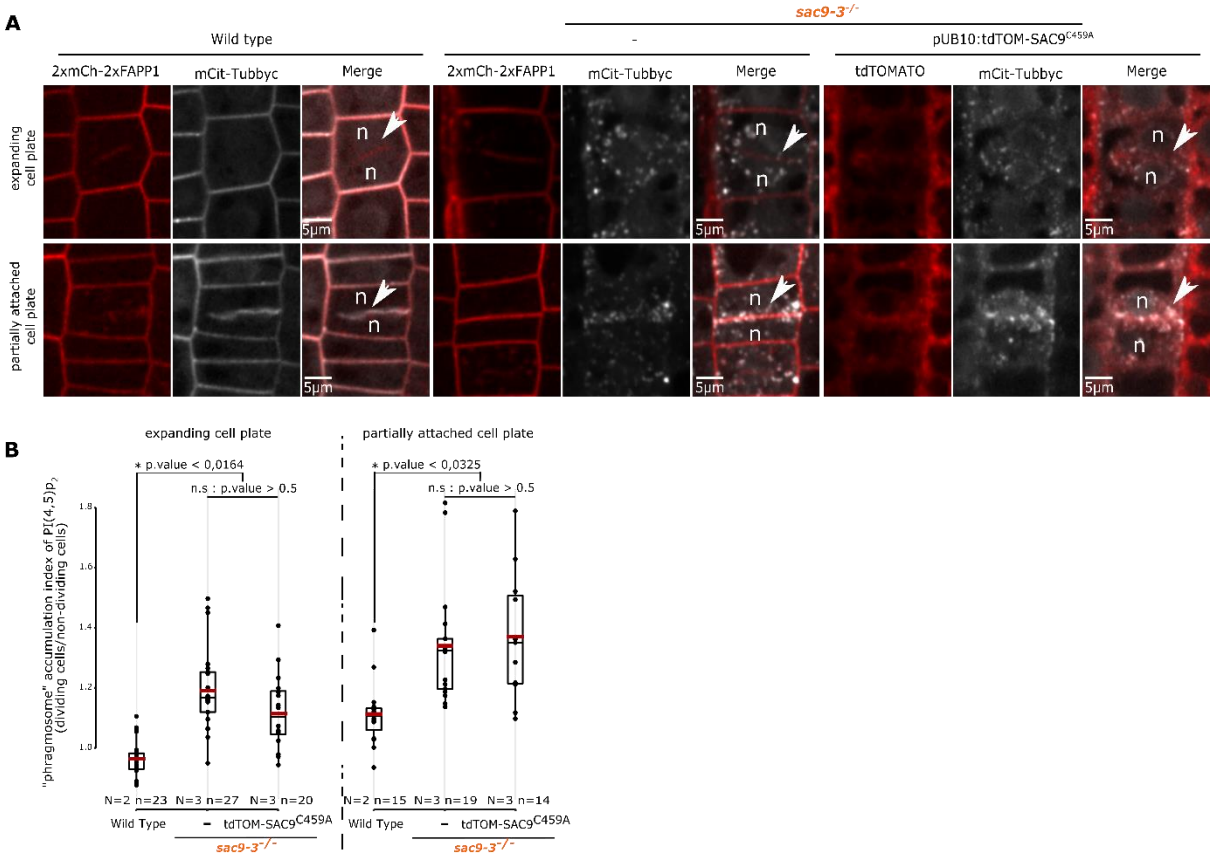

Fig. S6 | tdTOM-SAC9^{C459A} localization regarding the PI(4,5)P_2 biosensor during the discontinuous phragmoplast expansion in WT and *sac9-3*

A, Images of mCit-Tubbyc with tdTOM-SAC9^{C459A} in WT. **B**, Images of mCit-Tubbyc with tdTOM-SAC9^{C459A} in *sac9-3*. **C**, Normalized intensity profiles corresponding to (B) during the discontinuous phragmoplast phase. White arrow, PI(4,5)P_2 biosensor appearance; White arrowhead, abnormal PI4,5)P_2 enrichment at the leading zone in *sac9-3*; Yellow arrowhead, SAC9^{C459A} enrichment at the leading zone; White dotted line, cell contour; Blue arrow, cell plate fusion site; n, nucleus; Scale bars, 5µm.

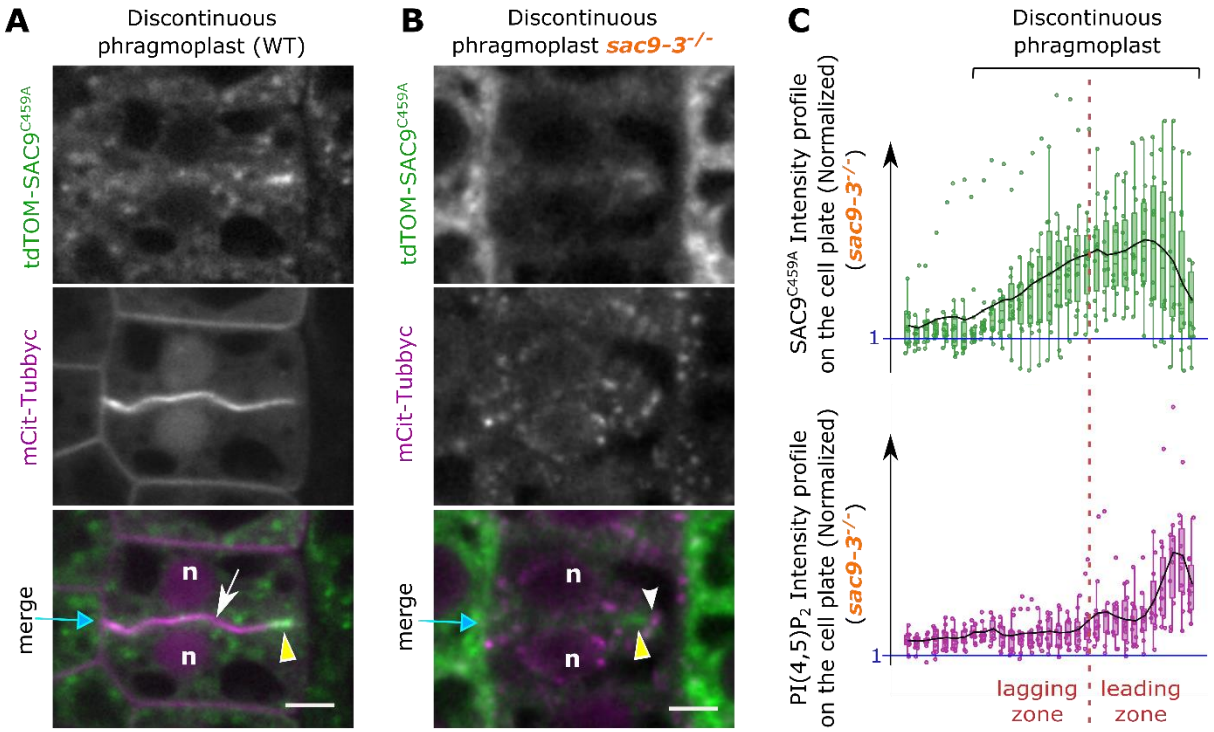

Fig. S7 | Mutation in the putative catalytic domain of SAC9 does not rescue the PI(4,5)P_2 biosensor misregulation during cell division.

A, Confocal images of WT expressing *2xmCh-PH^{FAPP1} (red)*, *sac9-3* expressing *2xmCh-PH^{FAPP1} (red)* and *sac9-3* expressing *tdTOM-SAC9^{C459A}*, together with *mCit-Tubbyc* (white). For the sets of three panels, the top images correspond to the "expanding cell plate" phase and the bottom image to the "partially attached cell plate" phase. Here, 2xmCh-2xPH^{FAPP1} is used as a marker for membranes (plasma membrane and cell plate). The white arrow points out the cell plate for PI(4,5)P_2, yellow arrowhead the SAC9^{C459A} enrichment and "n" the nucleus (scale bars, 5µm). **B**, Comparison of the phragmosome accumulation index for PI(4,5)P_2 biosensors (mCit-Tubbyc) at the "expanding cell plate" (left panel) and partially attached cell plate" (right panel) between WT, *sac9-3* mutant and *sac9-3* expressing *tdTOM-SAC9^{C459A}*. In the plots, middle horizontal bars represent the median, while the bottom and top of each box represent the 25th and 75th percentiles, respectively. At most, the whiskers extend to 1.5 times the interquartile range, excluding data beyond. For range of value under 1,5 IQR, whiskers represent the range of maximum and minimum values. Results of the statistical analysis (shown in the supplementary table) are presented (N = number of replicates, n = number of cells).

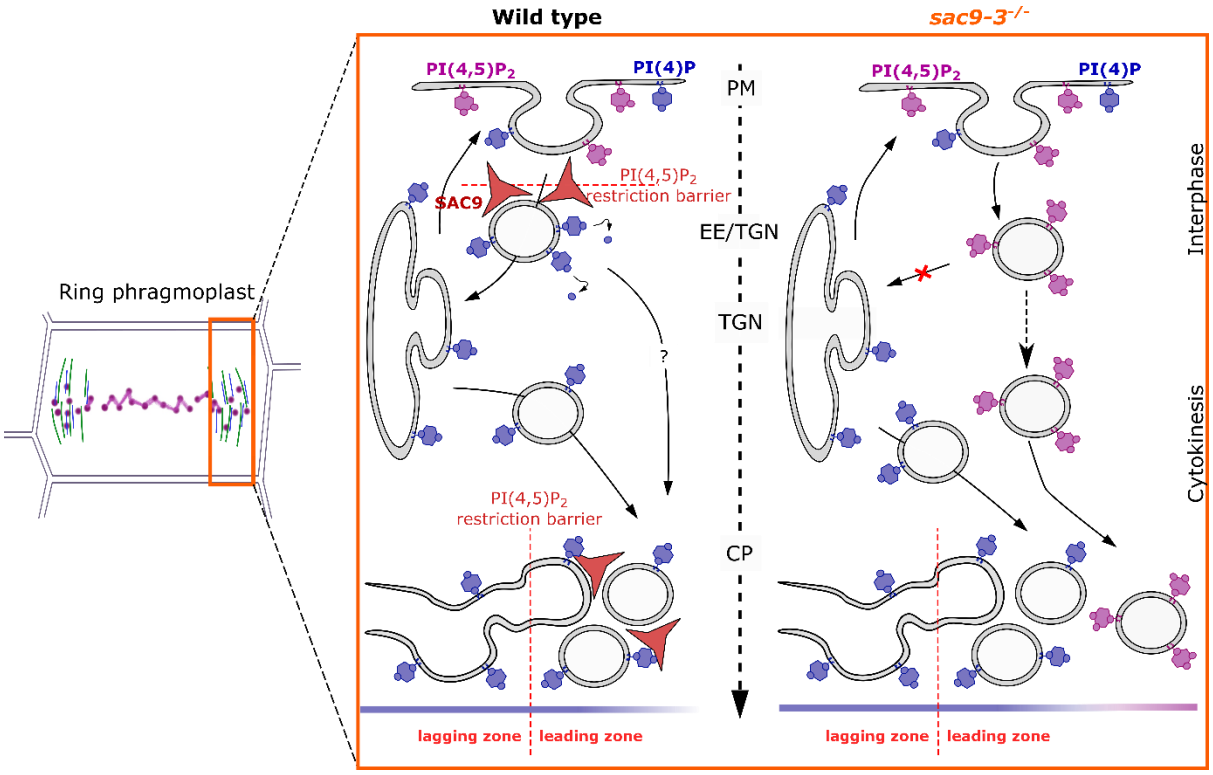

Fig. S8 | Model for the abnormal recruitment of PI(4,5)P_2 in *sac9-3* interphasic cells and mitotic cells

Hypothetical model of the mechanism at the cell plate edges based on our results. In wild-type plants, SAC9 restricts the PI(4,5)P_2 at the plasma membrane giving rise to a endomembrane system free of this lipid. Upon SAC9 absence, the PI(4,5)P_2 is accumulated in endomembrane compartments lost in the endocytic pathway, no longer able to reach and fuse to the TGN. This abnormal PI(4,5)P_2 containing membranes accumulating in absence of SAC9 are during the cytokinetic process directed at the leading edges of the phragmoplast where they particularly accumulated during its fusion to the plasma membrane.

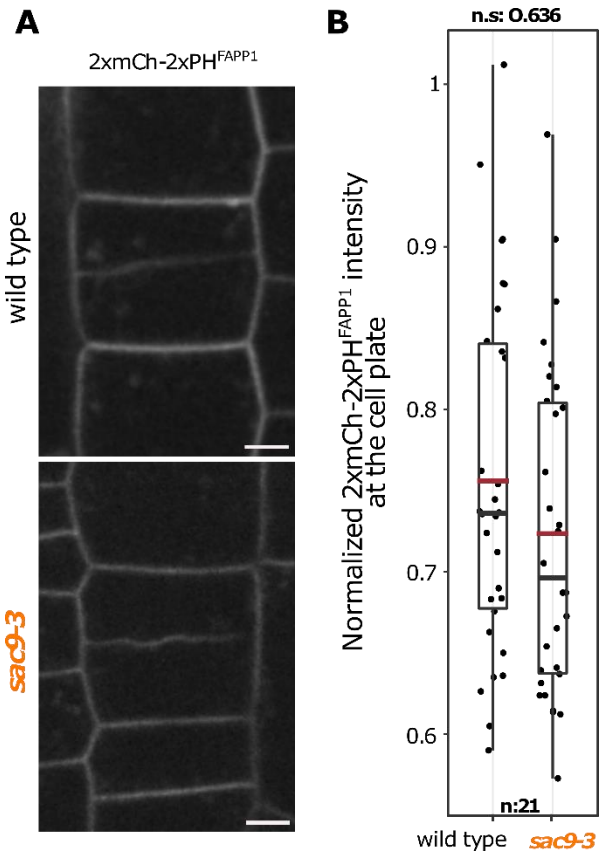

925

926 **<u>Fig. S9 | PI4P level at the cell plate is not significantly impacted in *sac9-3*.</u>**

927 **A**, Confocal images of 2xmCh-2xPH^{FAPP1}, PI4P reporter, during the final cell plate expansion (ring and
928 discontinuous phragmoplast) in wild type (upper panel) and *sac9-3* (bottom panel). **B**, comparison of
929 2xmCh-2xPH^{FAPP1} intensity at the cell plate, normalized by its intensity on the plasma membrane.

930

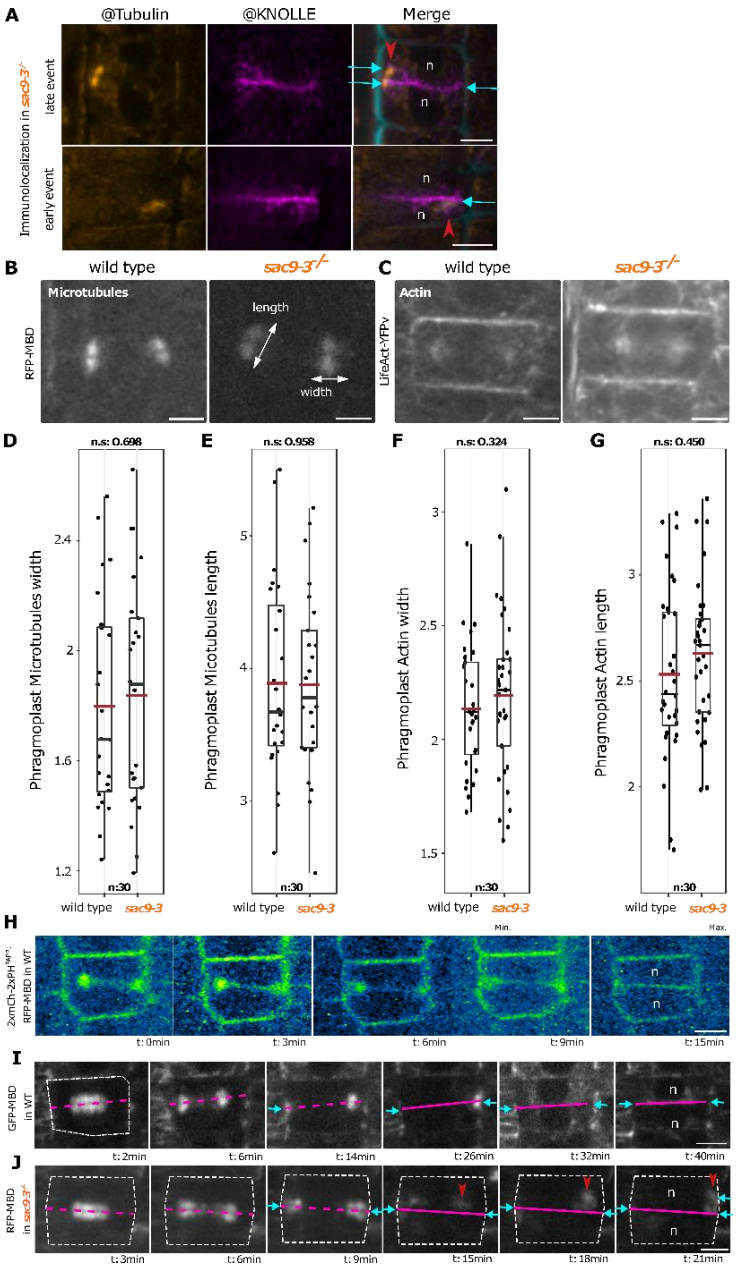

<u>Fig. S10 | In *sac9-3*, cell plate branching correlates with microtubule perturbation.</u>

A, Co-immunolocalization against αtubulin and KNOLLE in *sac9-3* stained with calcofluor during two steps of *sac9-3*'s defect emergence. Scale bar, 5 µm. **B**, Confocal images of microtubules, RFP-MBD in wild type (left) and *sac9-3* during the ring phragmoplast stage. **C**, Confocal images of actin filament, LifeAct-YFPv in wild type (left) and *sac9-3* during the ring phragmoplast stage. **D**, comparison of microtubules phragmoplast width. **E**, comparison of phragmoplast microtubules length. **F**, Comparison of Actin phragmoplast width. **G**, Comparison of Actin phragmoplast length **H**, Z projection of 2xmCh-2xPH^{FAPP1} and RFP-MBD in WT. Here, the signal is color coded in green fire blue (see scale bar on the right). The signal corresponding to microtubules and the one corresponding to membrane are not distinguished). Note that here, 2xmCh-2xPH^{FAPP1} is used at the membrane marker (plasma membrane and cell plate). **I**, Time-lapse of a Z projection of RFP-MBD in wild type. Scale bar, 5 µm. **J**, Time-lapse of a Z projection of RFP-MBD in *sac9-3*. Scale bar, 5 µm. Blue arrow, cell plate fusion site; White arrow, phragmoplast length and width; Red arrowhead, branched cell plate; n, nucleus.

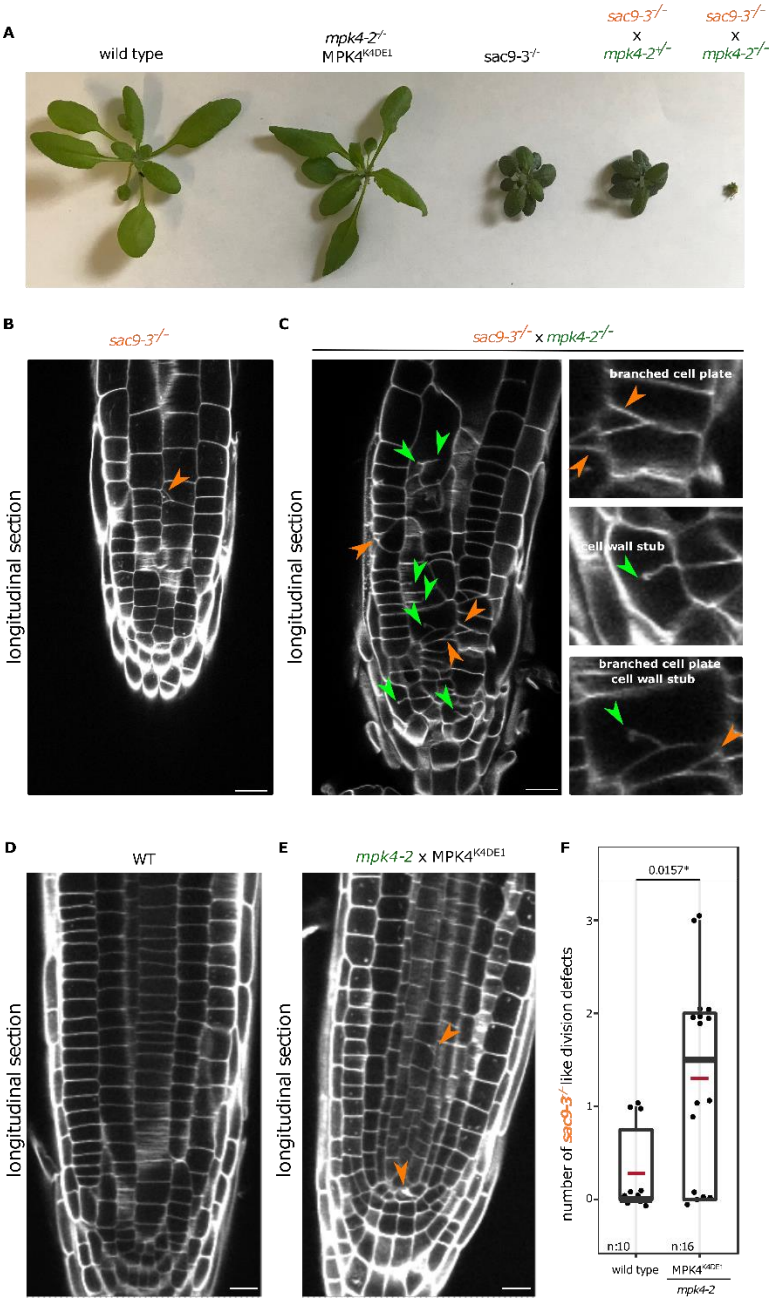

Fig. S11 | MPK4 activity could be part of *sac9-3* branching defect.

A and **B**, Representative image extracted from a Z-stack of calcofluor-stained fixed roots (21 day-olds) for *sac9-3* (a) and the double mutant *sac9-3 x mpk4-2* (B, left part: crop on defectives cells). **C** and **D**, Representative image extracted from a Z-stack of calcofluor-stained fixed roots (7 day-olds) for wild type (c) and *mpk4-2* complemented with a constitutively active MPK4 (MPK4^{K4DE1}). **E**, Quantification of the number of *sac9-3* like defects. The result of the statistical analysis (shown in the supplementary table) is presented. In the plots, middle horizontal bars represent the median, while the bottom and top of each box represent the 25th and 75th percentiles, respectively. At most, the whiskers extend to 1.5 times the interquartile range, excluding data beyond. For range of value under 1,5 IQR, whiskers represent the range of maximum and minimum values. Results of the statistical analysis (shown in the supplementary table) are presented (n = number of cells). Orange arrow, *sac9-3* like cell wall defects; Green arrow: cell wall stubs. Scale bar: 20 µM.

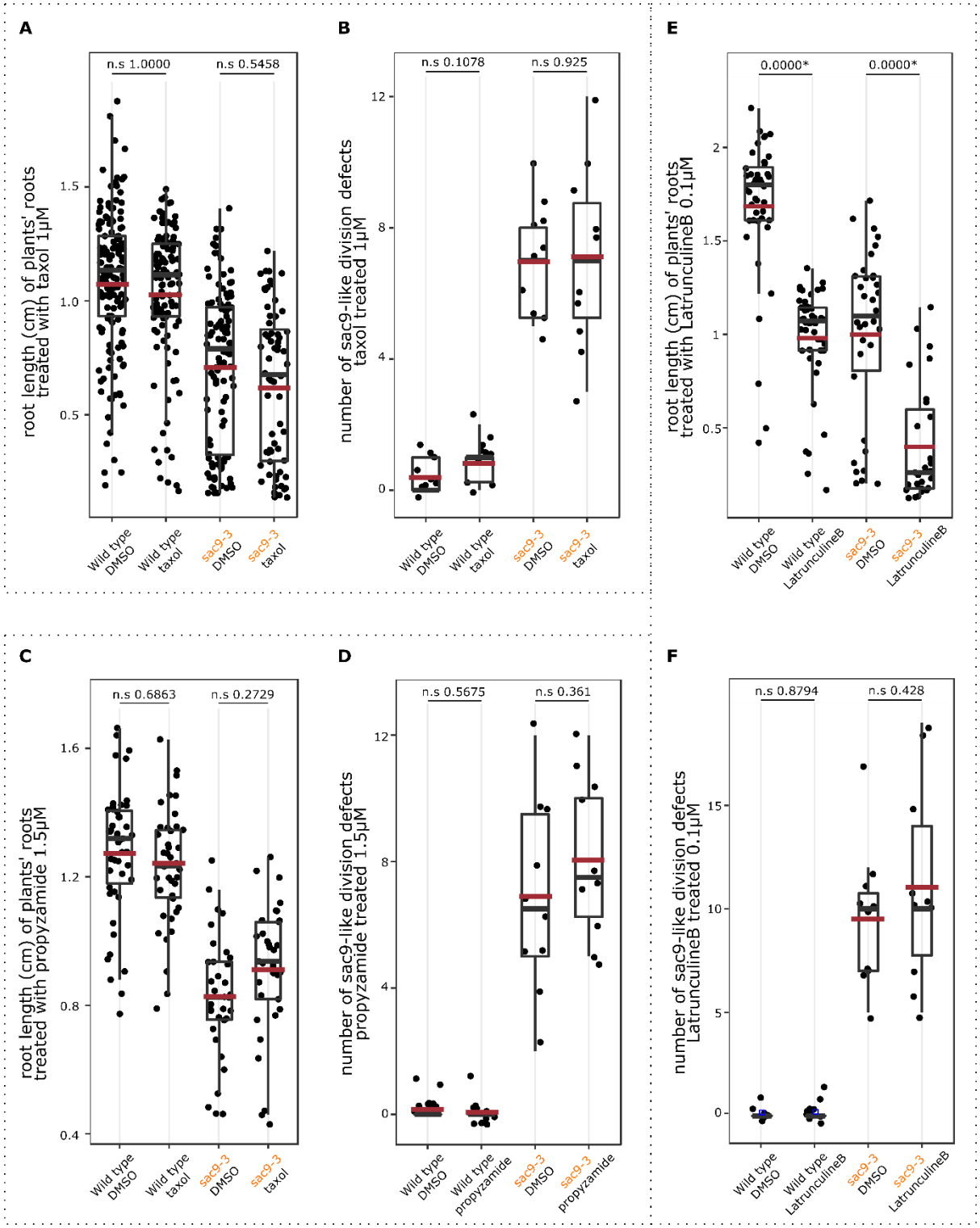

Fig. S12 | *sac9-3* mutant sensibility to mild cytoskeleton perturbation.

A, **B** Quantification at 7 days post germination (dpg) of WT and *sac9-3* root length grown on ½ MS plates supplemented with 1 µM Taxol (A) or 1.5 µM Propyzamide (B). **C**, **D** Quantification of *sac9-3* like division defects in 7 dpg WT and *sac9-3* plants grown on ½ MS plates supplemented with 1 µM Taxol (C) or 1.5 µM Propyzamide (D). **E** Quantification at 7 days post germination (dpg) of WT and *sac9-3* root length grown on ½ MS plates supplemented with 0.1 µM Latrunculin B. **F**, Quantification of *sac9-3* like division defects in 7 dpg WT and *sac9-3* plants grown on ½ MS plates supplemented 0.1 µM Latrunculin B.

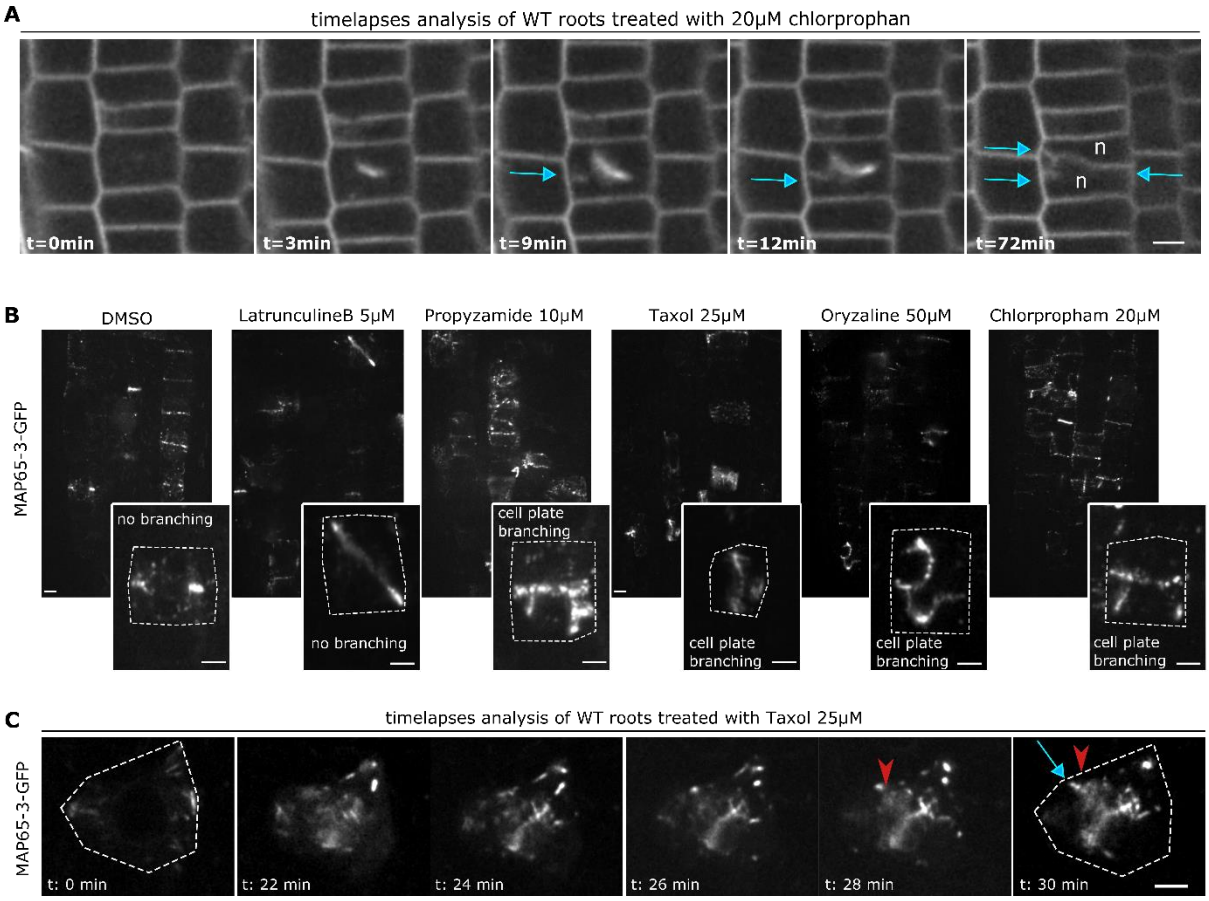

Fig. S13 | Pharmacological perturbation's of microtubules but not actin lead to cell plate branching, yet different from *sac9-3*.

A, image series acquired with a root tracking system of a wild type plant treated for 2 h with chlorpropham 20 µM. **B**, confocal images of wild type plants expressing *MAP65-3-GFP*, treated with (from left to right) 5µm Latrunculin B, 25µM Taxol, 10µM Propyzamide, 50µM Oryzalin and 20µM Chlorpropham respectively. **C**, Image series acquired with a root tracking system of a wild type plant expressing *MAP65-3-GFP* treated for 24 h with Taxol 25 µM. Scale bar, 5 µm. Blue arrow, cell plate fusion site; Red arrowhead, branched cell plate; n, nucleus.

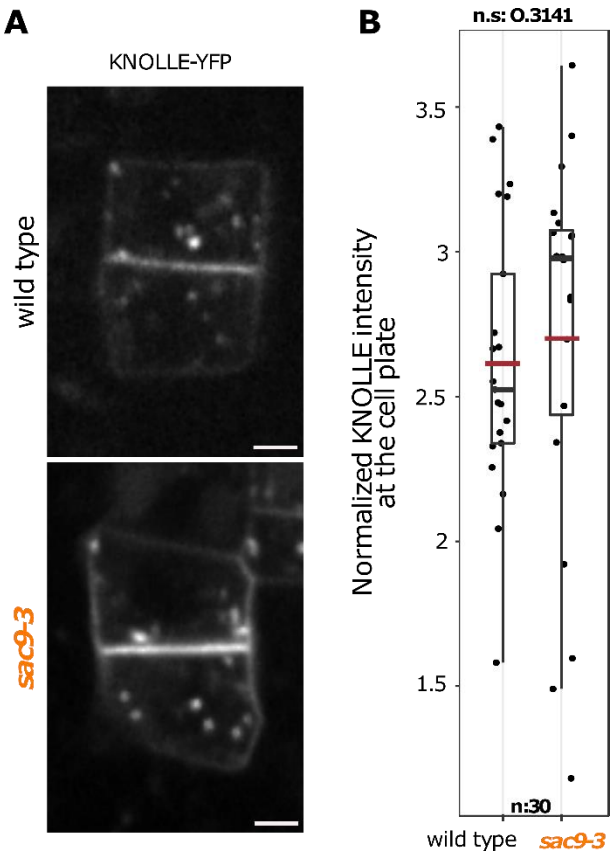

977

978 **<u>Fig. S14 | In *sac9-3*, no dispersed vesicular localization was observed for YFP-KNOLLE.</u>**

979 **A**, Confocal images of YFP-KNOLLE during the final cell plate expansion (ring and discontinuous
980 phragmoplast) in wild type (upper panel) and *sac9-3* (bottom panel). **B**, comparison of YFP-KNOLLE
981 intensity at the cell plate, normalized by its intracellular intensity.

982
983

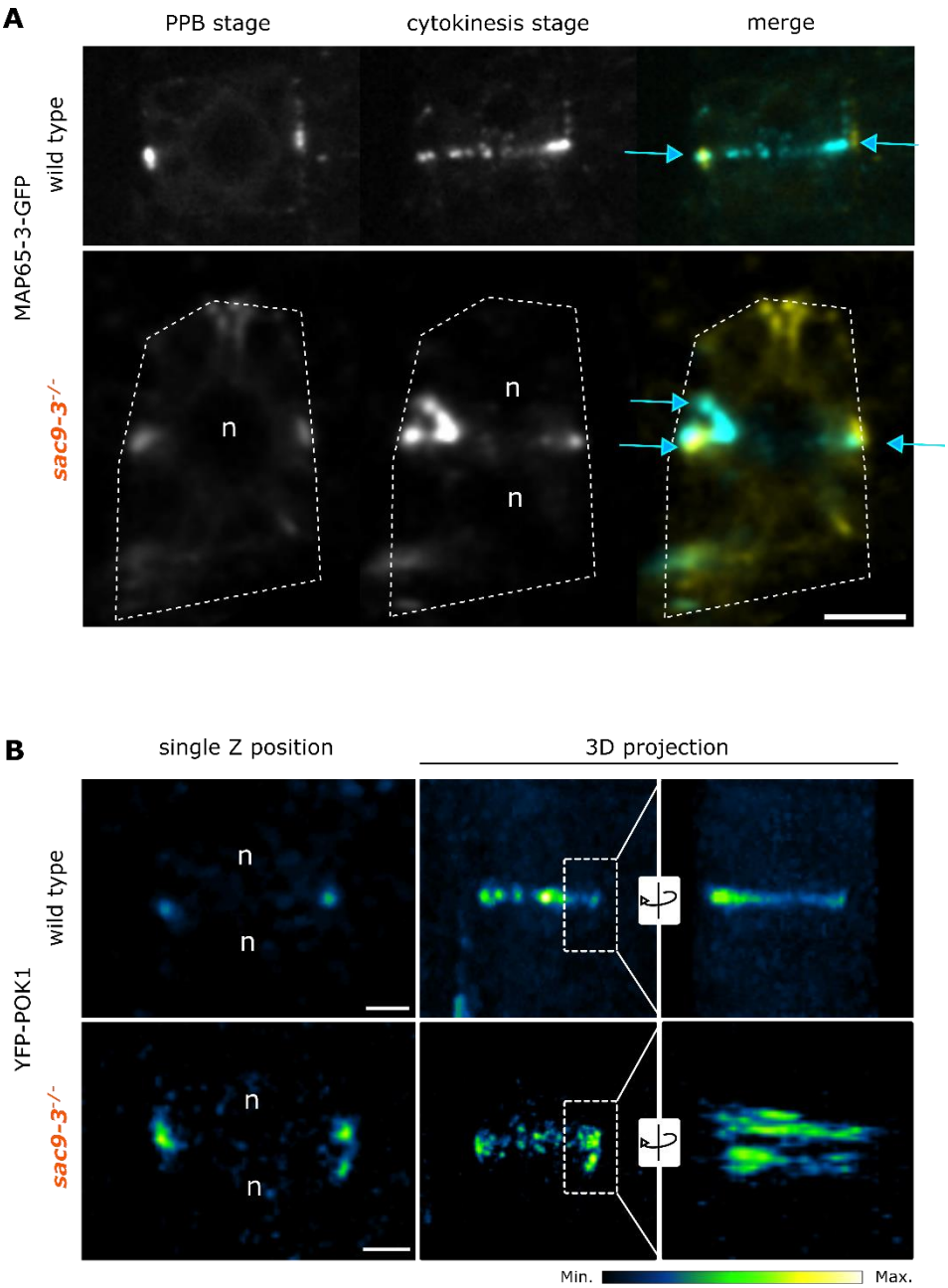

Fig. S15 | In *sac9-3*, cell plate branching correlates with a reorganization of the cortical division zone independently of the preprophase band.

A, Confocal images of the same cell expressing *MAP65-3-GFP* in wild type and *sac9-3* mutant at two different dividing steps (Pre-Prophase Band in yellow and cytokinesis in cyan). **B**, Images of YFP-POK1 in wild type and *sac9-3*. Left image represents a single optical section while the two other images are 3D projection and rotation of the cell. The signal is color coded in green fire blue (see scale bar). Scale bar, 5 µm. Blue arrow, cell plate fusion site.

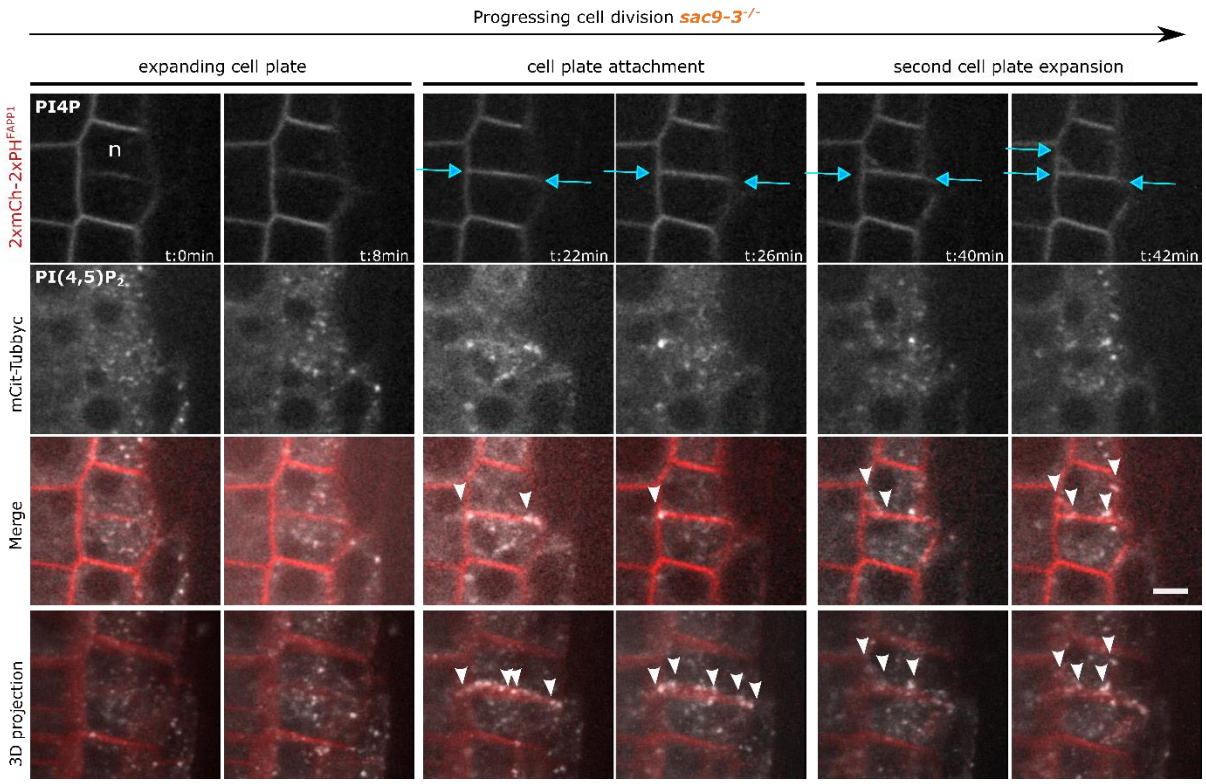

994

995 **Fig. S16 | In *sac9-3*, the PI(4,5)P_2 is abnormally recruited at the phragmoplast leading zone.**

996 Image series and 3D projection of an *in vivo* dividing *sac9-3* cells expressing both PI(4,5)P_2 (mCit-Tubbyc,
997 white) and PI(4)P (2xmCh-2xPH^{FAPP1}, red) biosensors. Images were taken every 2 min (between 20 and 30
998 Z-stack per frame) for 2 h with a root tracking system (*34*). Note that here, 2xmCh-2xPH^{FAPP1} is used at
999 the membrane marker (plasma membrane and cell plate). Blue arrow, cell plate fusion site; n, the nucleus;
1000 white arrowhead, in sac9-3, PI(4,5)P_2 biosensor "ring" surrounding the cell plate and PI(4,5)P_2 biosensor
1001 spot where the branch emerged and at its tip. Scale bars, 5 µm.

1002

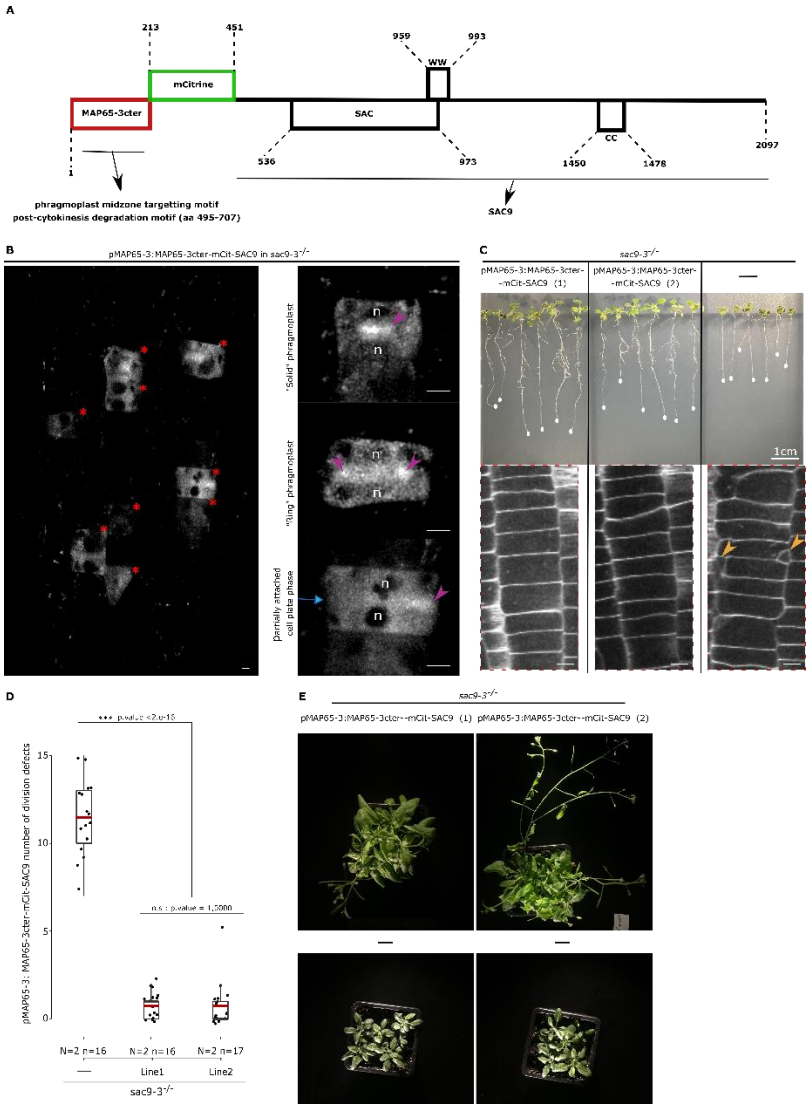

Fig. S17 | Partial rescue of *sac9-3* when SAC9 is only present in dividing cells.

A, Diagram representing the 2097 amino-acid MAP65-3^{cter}-mCit-SAC9 protein. We fused the C-terminal (Cter) domain of MAP65-3 that contains a microtubule binding site that enables specific activity in the phragmoplast midzone and its degradation post cytokinesis (*25*) to mCIT and SAC9 genomic sequence. **B,** left: Expression of *pMAP65-3:MAP65-3*^{cter}*-mCit-SAC9* in *sac9-3* dividing cells (red star) of the root meristematic zone. Right: localization of MAP65-3^{cter}-mCit-SAC9 at three cytokinesis steps. Scale bars, 5µm. **C**, Phenotypes of *sac9-3* (right panel) complemented with two MAP65-3^{cter}-mCit-SAC9 independent lines (middle and left panels). Top panel: representative images of the macroscopic phenotype observed (21dpi); Bottom panel: images of calcofluor-stained fixed roots (10 day-old). Scale bars, 5µm. Orange arrowhead, division defects; n, nucleus; yellow arrowhead, enrichment on the cell plate; Blue arrow, the cell plate fusion site. **D**, Quantification of the number of division defects in *sac9-3* and *sac9-3* expressing *MAP65-3:MAP65-3*^{cter}*-mCit-SAC9*. In the plots, middle horizontal bars represent the median, while the bottom and top of each box represent the 25th and 75th percentiles, respectively. At most, the whiskers extend to 1.5 times the interquartile range, excluding data beyond. For range of value under 1,5 IQR, whiskers represent the range of maximum and minimum values. Results of the statistical analysis (shown in the supplementary table) are presented (N = number of replicates, n = number of cells). **E**, Representative images of the aerial phenotype observed (6-week-old plants).

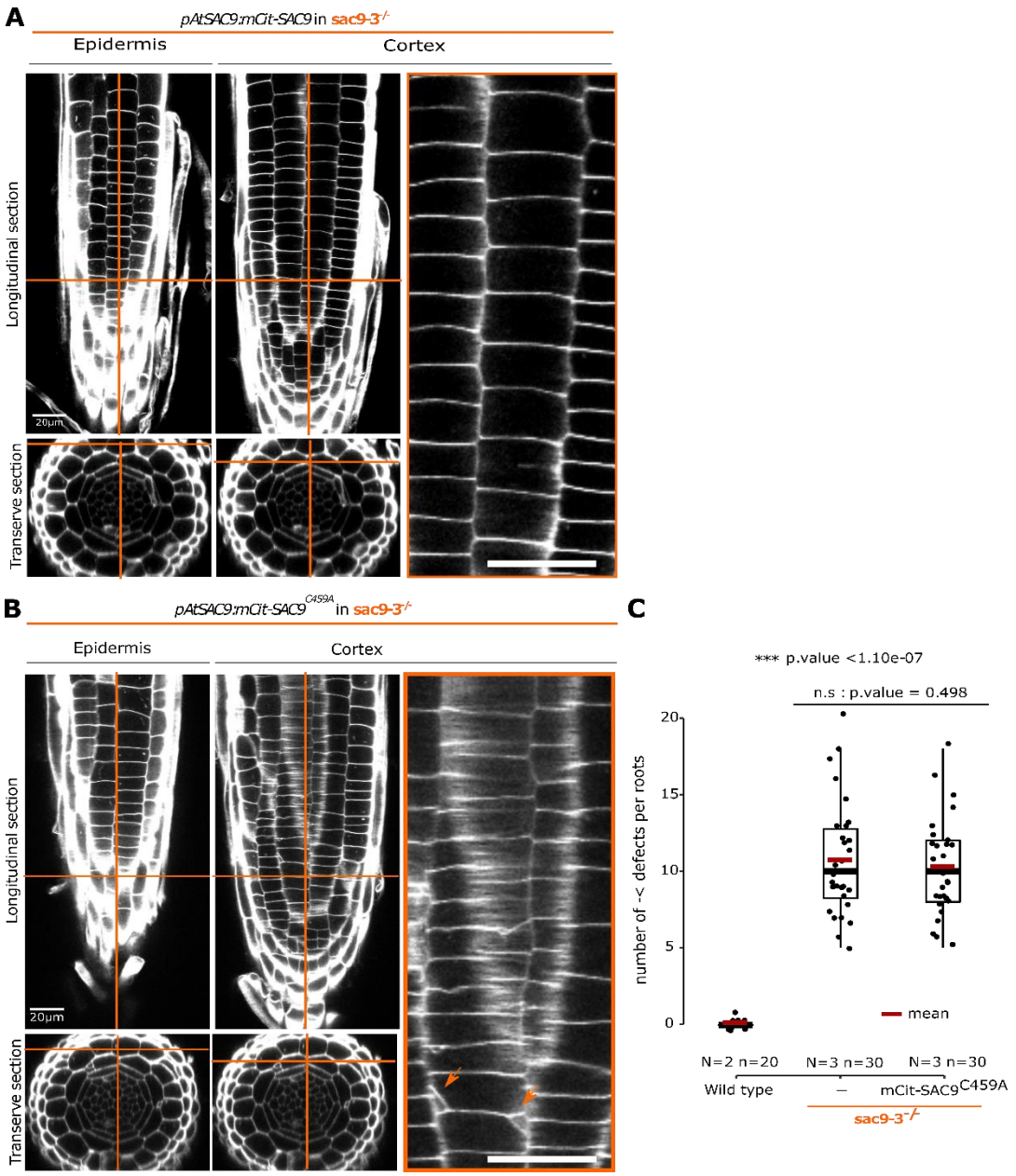

Fig. S18 | Mutation in the putative catalytic domain of SAC9 does not rescue the phenotype during cell division.

A, B, Z-stack images of calcofluor-stained fixed roots (7-day-old) *sac9-3* expressing the functional *mCit-SAC9* (A), *mCit-SAC9*^{C459A} (B). The left panel shows the epidermis layer in a longitudinal section (top, scale bar 20 µm.) and a transverse section (bottom). The middle panel shows the cortex layer, in the same way as the epidermis. The right panel shows a crop of the cortex layer (scale bar 5 µm). Orange arrow, cell division defects; Orange cross-section, position within the tissue for longitudinal and transverse sections. **C**, Quantification of the number of cell wall defects in wild-type, *sac9-3* and mCit-SAC9^{C459A} in *sac9-3*. In the plots, middle horizontal bars represent the median, while the bottom and top of each box represent the 25th and 75th percentiles, respectively. At most, the whiskers extend to 1.5 times the interquartile range, excluding data beyond. For range of value under 1,5 IQR, whiskers represent the range of maximum and minimum values. Results of the statistical analysis (shown in the supplementary table) are presented (N = number of replicates, n = number of cells).

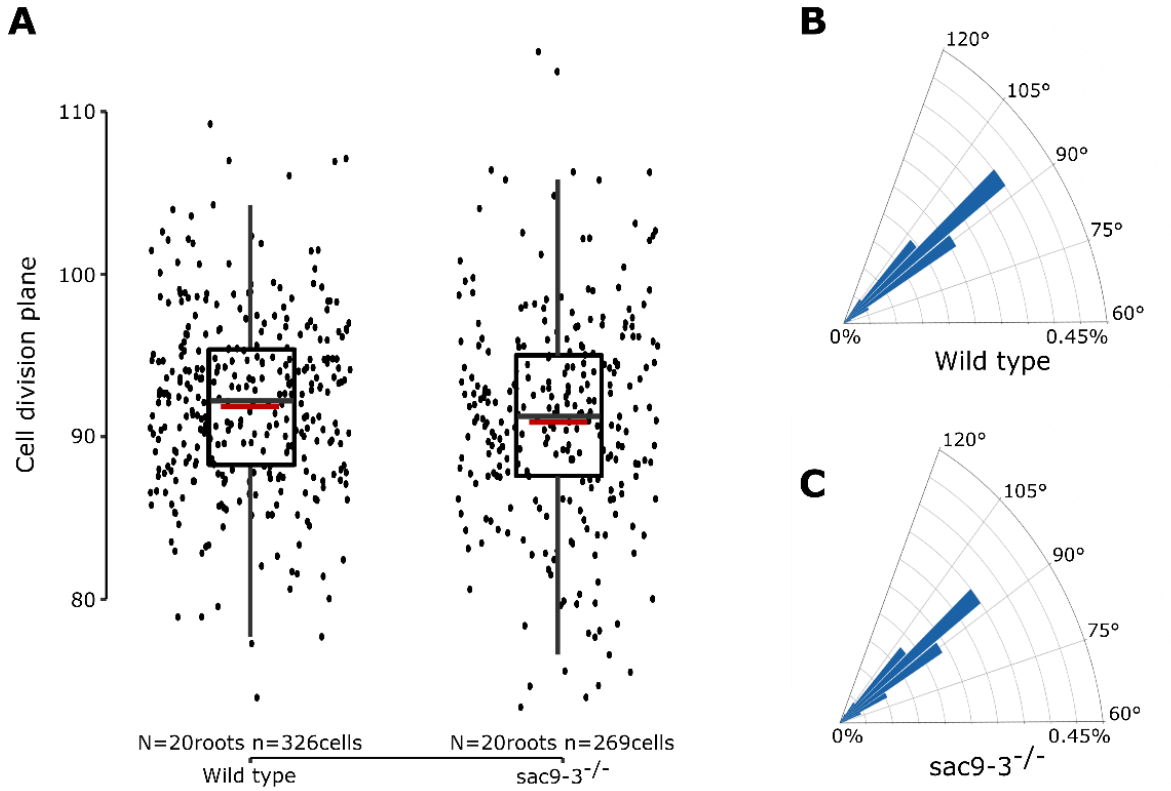

Fig.S19 | division plane comparison between wild type and sac9-3 mutant.

A, Comparison of division plane orientation in cortex cells (relative angle between the transverse cell wall and the root growth axis) between wild type and sac9-3 plants. In the plots, middle horizontal bars represent the median, while the bottom and top of each box represent the 25th and 75th percentiles, respectively. At most, the whiskers extend to 1.5 times the interquartile range, excluding data beyond. For range of value under 1,5 IQR, whiskers represent the range of maximum and minimum values. red bars represent the mean value. B, C, representation of cell wall angle for respectively wild type and sac9-3 plants.

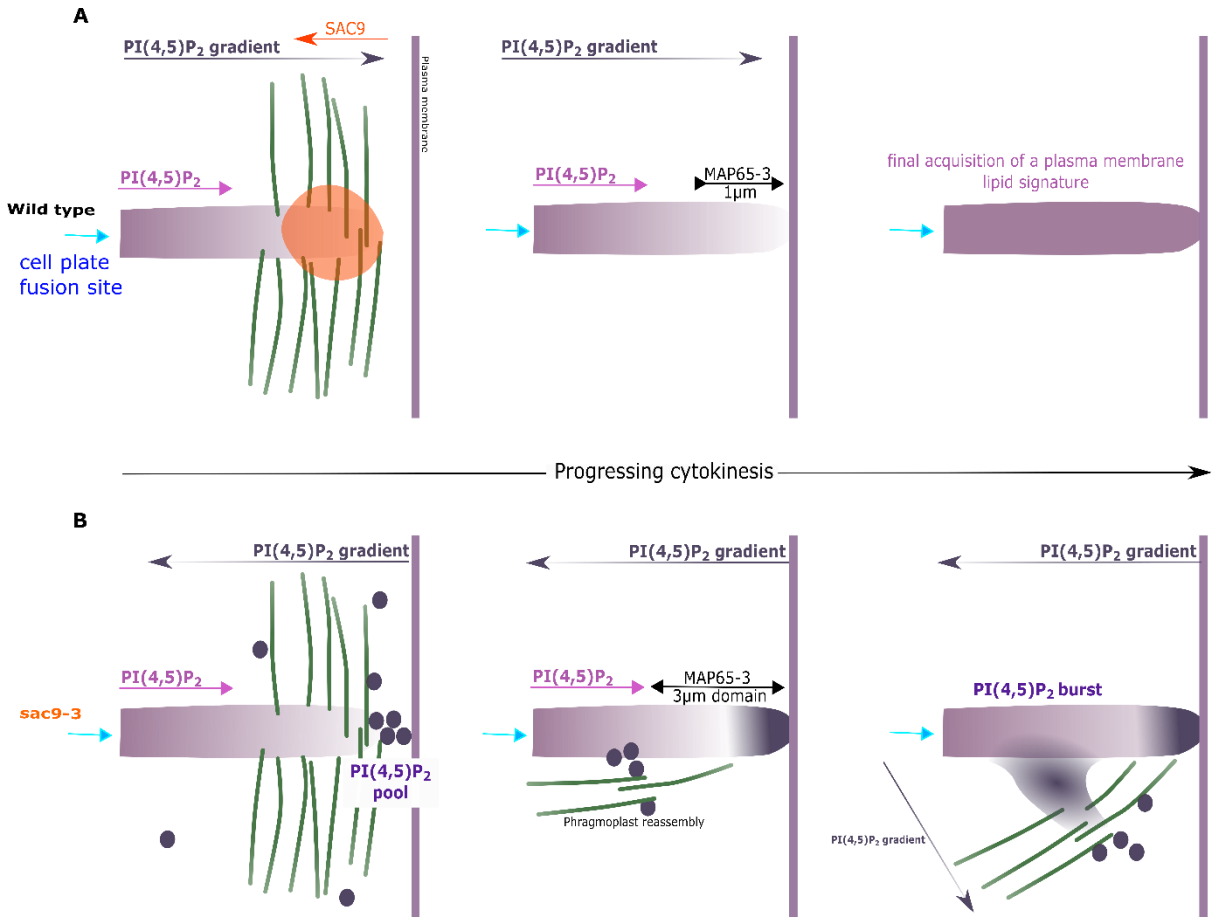

Fig. S20 | Proposed model

A, Concomitantly to the final cell plate attachment to the mother cell, PI(4,5)P_2 gradually invades the entire plasma membrane precursor from the maturing zone to the decreasing leading zone. This PI(4,5)P_2 patterning is tightly controlled through the action of SAC9 enzyme, directly at the cell plate or in endosomes surrounding the not yet attached cell plate leading zone. **B**, In *sac9* mutant, the abnormal accumulation of PI(4,5)P_2-rich endosomes close to the cell plate leading edge influences cell plate growth. Alternatively, the aberrant PI(4,5)P_2 patterning in sac9-3 might be perceived by the cytokinetic apparatus as in the opposite direction relative to the cell plate growth direction, creating a conflict in the spatial coordination of the expanding leading zone. In any case, mis-localized PI(4,5)P_2 in *sac9* lead to a MAP65-3 ~ 3 µm domain stabilization, even after cell plate complete attachment, and second to reassembly of the phragmoplast apparatus on the inner side of the MAP65-3 domain. Following phragmoplast reassembly, a cell plate protuberance emerges and expands toward the plasma membrane, with a precise geometry.

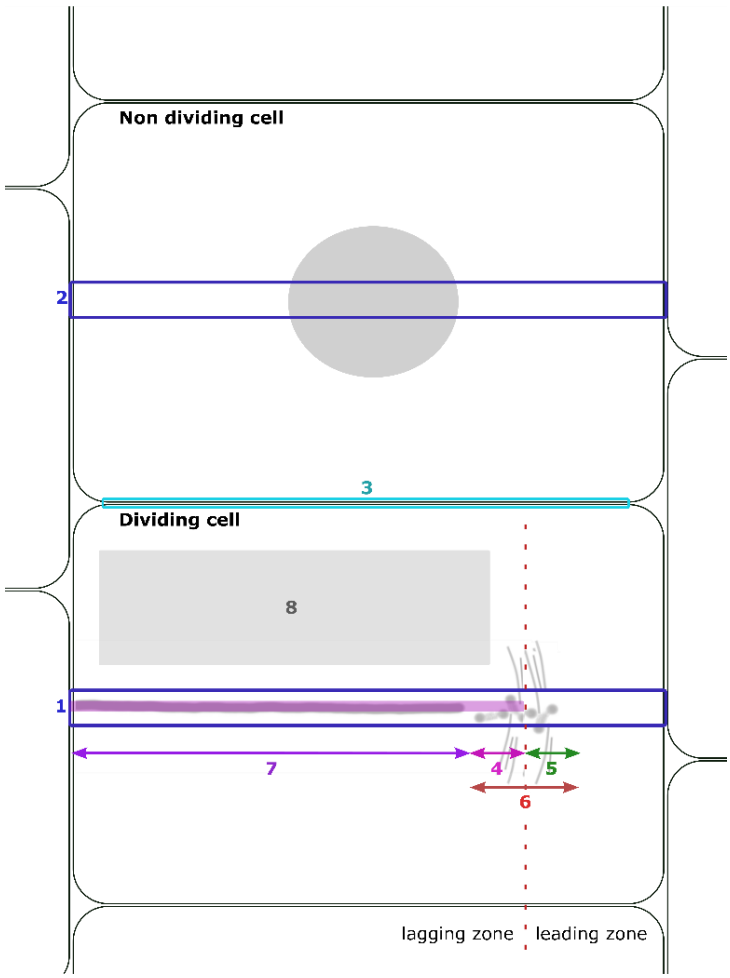

Fig.1F, fig.S3

$$\frac{\text{(cell plate lagging (4) or leading (5) zone intensity - cytosolic background (8))}}{\text{(phragmoplast midzone intensity (6) -cytosolic background (8))}}$$

Fig.2C, F

$$\frac{\text{cell plate lagging (4) or leading (5) zone intensity}}{\text{cell plate center intensit (7)}}$$

fig.S6

$$\frac{\text{"phragmosome" intensity of a dividing cell (1) /plasma membrane intensity (3)}}{\text{"phragmosome" intensity of a \textbf{non} dividing cell (2) /plasma membrane intensity (3)}}$$

fig.S9

$$\frac{\text{cell plate center intensit (7)}}{\text{plasma membrane intensity (3)}}$$

fig.S14

$$\frac{\text{cell plate center intensit (7)}}{\text{cytosolic background (8)}}$$

Fig. S21 | Quantification methods

Graphical representation of one dividing cell (at the discontinuous phragmoplast stage) and one non-dividing cell to illustrate the intensity quantification made on this paper. Critical zones are highlighted by arrows as well as the equations used.

1066 **Movie S1**| Colocalization analysis of tdTOM-SAC9^{C459A} (magenta) with MAP65-3-GFP (green)
1067 Time-course analysis during cytokinesis of tdTOM-SAC9^{C459A} (magenta) with MAP65-3-GFP (green) using
1068 a root tracking system (*34*). The division was imaged every two minutes. Scale bar, 5μm

1069 **Movie S2** | PI(4,5)P_2 behavior during cytokinesis in *sac9-3* mutant
1070 Time-course analysis using a root tracking system (*34*) of mCit-Tubbyc (white) and 2xmCH-2xPH^{FAPP1}
1071 (red) subcellular localization during cytokinesis in *sac9-3*. Here, 2xmCh-2xPH^{FAPP1} is used as a marker for
1072 membranes (plasma membrane and cell plate). The division was imaged every two minutes. Scale bar: 5
1073 μm.

1074 **Movie S3** | MAP65-3-GFP behavior during cytokinesis in wild-type plants
1075 Time-course analysis using a root tracking system (*34*) of MAP65-3-GFP subcellular localization during
1076 cytokinesis in WT. The division was imaged every two minutes. Scale bar : 5μm

1077

1078 **Movie S4 and S5** | MAP65-3-GFP behavior's during cytokinesis in *sac9-3*
1079 Example of defective cytokinesis in *sac9-3* expressing *MAP65-3-GFP* and imaged over time using a root
1080 tracking system (*34*). The division was imaged every two minutes. scale bar: 5 μm

1081

1082 **Movie S6** |Mild treatment with chloropropham induces cell plate branching
1083 Time-course analysis using a root tracking system of the plasma membrane labeling PI4P biosensor (mCIT-
1084 P4M) in WT root treated for 2 h with chlorpropham. Here, mCIT-P4M is used as a marker for membranes
1085 (plasma membrane and cell plate). Scale bar: 10 μm

1086

1087 **Movie S7** | Imaging of the defects during cytokinesis in *sac9-3*
1088 Time-course analysis using a root tracking system (*34*) of 2xmCH-2xPH^{FAPP1} in *sac9-3* during cell plate
1089 defect formation (arrow). Here, 2xmCH-2xPH^{FAPP1} is used as a marker for membranes (plasma membrane
1090 and cell plate). Scale bar: 5 μm

1091

1092 **Movie S8** | branched cell wall defects segmentation in *sac9-3*
1093 Rotation of a branched cell wall defect (green) and its neighboring cell (gray) 3D view imaged after
1094 calcofluor staining.

1095

1096 **Movie S9** | branched cell wall defects segmentation in *sac9-3*

1097 Rotation of branched cell wall defects accumulation (green) and their neighboring cell (gray) 3D view
1098 imaged after calcofluor staining.

1099

1100 **Movie S10** | $PI(4,5)P_2$ behavior during double cell plate attachment in *sac9-3*

1101 Time-course analysis using a root tracking system (*34*) of mCit-Tubbyc (white) and 2xmCH-2xPH^{FAPP1}
1102 (red) subcellular localization during cytokinesis in *sac9-3*. Here, 2xmCH-2xPH^{FAPP1} is used as a marker for
1103 membranes (plasma membrane and cell plate). The division was imaged every two minutes. Scale bar, 5µm

1104

1105 **Supplementary tables** | Resources and statistics.

1106 A, Reagent and resources. B, Details of the statistics corresponding to Fig. 1F. C, Details of the statistics
1107 corresponding to Fig. 2C, 2F. D, Details of the statistics corresponding to Fig. 5B. E, Details of the statistics
1108 corresponding to Fig. 6B. F, Details of the statistics corresponding to fig. S3B, S3D. G, Details of the
1109 statistics corresponding to fig. S6B. H, Details of the statistics corresponding to fig. S9B. I, Details of the
1110 statistics corresponding to fig. S10D, S10E, S10F, S10G. J, Details of the statistics corresponding to fig.
1111 S11F. K, Details of the statistics corresponding to figure S12A to S12F. L, Details of the statistics
1112 corresponding to fig. S14B. M, Details of the statistics corresponding to fig. S17D. N, Details of the
1113 statistics corresponding to fig. S18C.